Identifying Space-Resolved Proteins of the Murine Thymus, by Combining MALDI Mass Spectrometry Imaging and Proteomics

Jennifer T. Aguilan[1,2], Carlos Madrid-Aliste[2,3], Joshua Fischer[4], Simone Sidoli[2,5,†], George S. Karagiannis[4,6,7,8,9,10,†]

[1]Department of Pathology, Albert Einstein College of Medicine, Bronx, NY, USA

[2]Laboratory for Macromolecular and Proteomics Facility, Albert Einstein College of Medicine, Bronx, NY, USA

[3]Department of Systems and Computational Biology, Albert Einstein College of Medicine, Bronx, NY, USA

[4]Bruker Daltonics Corporation, New York, USA

[5]Department of Microbiology & Immunology, Albert Einstein College of Medicine, Bronx, NY, USA

[6]Department of Biochemistry, Albert Einstein College of Medicine, Bronx, NY, USA

[7]Gruss-Lipper Biophotonics Center, Albert Einstein College of Medicine, Bronx, NY, USA

[8]Tumor Microenvironment Program, Montefiore-Einstein Comprehensive Cancer Center, Bronx, NY, USA

[9]Integrated Imaging Program for Cancer Research, Montefiore-Einstein Comprehensive Cancer Center, Bronx, NY, USA

[10]Cancer Dormancy Institute, Montefiore-Einstein Comprehensive Cancer Center, Bronx, NY, USA

[11]Marilyn and Stanely M. Katz Institute for Immunotherapy for Cancer and Inflammatory Disorders, Montefiore-Einstein Comprehensive Cancer Center, Bronx, NY, USA

[†]Indicates co-corresponding authorship

ABSTRACT

The ability to identify spatially resolved proteomes has advanced markedly in recent years, yet integrating definitive protein identification with precise spatial localization in a single workflow remains a challenge. Matrix-assisted laser desorption/ionization mass spectrometry imaging (MALDI-MSI) enables antibody-free mapping of proteins directly in tissue sections, but its capacity for unambiguous protein identification is limited. Here, we present a combined MALDI-MSI and liquid chromatography-tandem mass spectrometry (LC-MS/MS) approach, to map protein localization, and track spatial changes in murine thymus during chemotherapy-induced involution and regeneration. Our workflow incorporates a scoring algorithm (pepBridge) that aligns MALDI-MSI molecular signals with LC-MS/MS identifications, enabling confident assignment of proteins that are critical to thymic function. Using this pipeline, we reveal spatiotemporal changes in proteins involved in cell migration, cytoskeletal remodeling, and endogenous thymic regeneration. Notably, we identify distinct spatial shifts in Nucleoprotein TPR and Tubulin-associated chaperone A (TBCA), corresponding to chemotherapy-driven architectural remodeling. From a translational perspective, these findings highlight pathways and candidate targets to promote immune recovery in pediatric cancer patients undergoing cytoreductive therapy. Analytically, this framework advances spatial proteomics by enabling high-confidence protein identification in lymphoid and other tissues, broadening the potential of translational proteomic research.

Keywords: imaging, mass spectrometry, thymus, chemotherapy, involution, regeneration

INTRODUCTION

The identification of spatially resolved proteomes has been a challenge that only recently met some breakthroughs (Mund A et al, 2022). While advanced instrumentation and time-consuming protocols can identify proteomes to resolve single-cell identity and heterogeneity, imaging mass spectrometry experiments are still met with limitations in combining protein identification with respective localization in a single experimental run. Matrix assisted laser desorption ionization - mass spectrometry imaging (MALDI-MSI) is a technique that circumvents such issues. MALDI-MSI can perform spatial mapping of peptides or proteins directly on a flash frozen or formalin-fixed paraffin-embedded (FFPE) tissue section. One main advantage of MALDI-MSI over traditional immunohistochemistry is that it does not require antigen-specific antibodies to map locations of peptides or proteins on the tissue. Therefore, it is a very useful molecular histology tool for both screening and multiple detection of potential new biomarkers for diseases. However, MALDI-MSI is generally limited due to the low signal-to-noise ratio (Gonzalez-Fernandez A et al, 2023) and the limited capability of performing MS/MS fragmentation of candidates, which reduces the specificity of detection (Buchberger AR et al, 2018). Other limitations of MALDI-MSI include the absence of chromatographic separation, which often results in a bias toward detecting the most abundant proteins, and the use of linear TOF mass analyzers for intact protein imaging, which can lead to detector saturation and a limited effective mass range typically up to ~30 kDa, with a theoretical maximum near 100 kDa.

In this work, we used MALDI-MSI as an unbiased approach for resolving organ/tissue compartmentalization by studying differential expression of proteins through on-tissue peptide spatial mapping. To serve these needs, we adopted an established mouse model of acute thymic involution (Hun ML et al, 2020), an organ pathology for which MALDI-MSI has not been previously used to extrapolate biological insights. We focused on the thymus, a central lymphoid organ critical for T cell development. While MALDI-MSI has been applied to thymus tissue previously for metabolite mapping (Tsuji Y et al, 2021), lipid imaging (Denti V et al, 2021), and calcitriol mapping (Meyer et al. 2024), it has not yet been used to map the proteome of the thymus, to our knowledge. Thus, our study provides a first look at thymic protein distributions via MALDI-MSI, combined with LC-MS/MS identification.

Combining MALDI-MSI with LC-MS/MS-based identification is an approach with significant precedent in the literature. For instance, Lemaire et al. (2007) (Lemaire R et al, 2007) pioneered on-tissue trypsin digestion followed by LC-MS/MS of tissue extracts to identify proteins observed by MALDI imaging. Later, Fáta et al. (2016) (Fata CR et al, 2015) and Quanico et al. (2017) (Quanico J et al, 2017) presented variations of the protocol. In 2020, Dewez et al. (Dewez F et al, 2020) introduced laser microdissection guided by MSI in the procedure. More recent efforts (Guo et al., 2021) have introduced software for automating such integrations with false discovery controls. Our work builds upon this foundation: we apply the approach to mapping the murine thymus proteome, an organ not previously profiled by MALDI-MSI in a proteomic context, and we introduce a scoring-based informatics pipeline (pepBridge) to facilitate peptide matching on a lower-resolution MALDI-TOF platform. The novelty of our study thus lies in the specific biological insights into thymus regeneration and the tailored computational method.

The thymus is a primary lymphoid organ of T cell development and functional maturation and sits encapsulated above the heart in the mediastinum. The thymus consists of two lobes that divide into lobules, which in turn, are subdivided into two distinct zones, an outer cortex and an inner medulla. These compartments embody functional “niches” that provide essential spatiotemporal signals that regulate key processes of T cell development, in particular thymocyte homing, survival and expansion, as well as T cell receptor chain rearrangement, and the establishment of central tolerance. In both embryonic and non-embryonic thymi, these

processes are spatially orchestrated by an intrathymic stromal network of cortical (cTEC) and medullary (mTEC) thymic epithelial cells, as well as by a supporting network of non-epithelial stromal cells, such as fibroblasts, blood vessel endothelial cells and their associated pericytes, etc. All these stromal cells, either epithelial or non-epithelial, reside in and specialize their functions in distinct cortical and medullary thymic compartments (Abramson J & Anderson G, 2017, Alawam AS et al, 2020, Anderson G & Takahama Y, 2012, Bhalla P et al, 2022, Cabric V & Brown CC, 2023, Chidgey AP & Boyd RL, 2001, Han J & Zuniga-Pflucker JC, 2021, James KD et al, 2021, Kadouri N et al, 2020, Kato S, 1997, Manley NR et al, 2011, Munoz JJ et al, 2009, Nitta T, 2022, Owen JJ et al, 2000, Sun Q et al, 2021, Takahama Y et al, 2017).

During preadolescence, the thymus plays an essential role in establishing a comprehensive and enduring T cell repertoire, which is pivotal for systemic immunity, immune surveillance, and the establishment of central tolerance (Baran-Gale J et al, 2020, Cahill RN et al, 1997, Webb S & Haniffa M, 2023). Notably, this period marks the zenith of the thymus functional capacity, which subsequently experiences a progressive, age-related decline. By early adulthood, the reliance of systemic immunity on the thymus decreases, shifting towards increased dependence on the expansion of peripheral memory T cells (Aw D et al, 2009, Minato N et al, 2020, Ostan R et al, 2008, Palmer DB, 2013, Palmer S et al, 2018, Rane S et al, 2022). More importantly, the thymus is particularly vulnerable to a variety of cytotoxic agents, leading to its rapid (acute) thymic involution (ATI) (Ansari AR & Liu H, 2017, Chaudhry MS et al, 2016, Kinsella S & Dudakov JA, 2020, Lagou MK et al, 2022, Swami S et al, 2012, Yang H et al, 2009). For instance, treatment of cancer patients with cytoreductive chemotherapy leads to both short- and long-term consequences on systemic immunity, in part due to ATI (Ansari AR & Liu H, 2017, Fletcher AL et al, 2009, Kinsella S & Dudakov JA, 2020, Lagou MK et al, 2022, Wertheimer T et al, 2018). Given the key role of the thymus in immune development in children, ATI emerges as pressing concern for pediatric cancer patients undergoing cytoreductive treatments, thus necessitating meticulous consideration to alleviate its effects on systemic immunity. Administration of chemotherapy and radiotherapy exacerbates ATI and compromises the immune system, making pediatric patients vulnerable to infections, and challenging immune system recovery post-therapy (Ansari AR & Liu H, 2017, Lagou MK et al, 2022). Strategies aimed at fostering endogenous thymic regeneration during or after chemo/radiotherapy hold the promise of significantly improving life expectancy and quality-of-life for pediatric cancer survivors. However, progress in understanding thymic recovery post-cytotoxic treatment has been limited, especially due to the lack of systemic approaches like single-cell transcriptomics and high-throughput proteomics. Advancing these techniques in this field could significantly enhance our ability to restore immune functions and competence in pediatric cancer patients.

In addition, given the histological perplexities of lymphoid organs such as the thymus, it is imperative to implement spatial resolution in such sophisticated analytical techniques, to be able to gain sufficient and valuable information for complicated immune responses. Given that MALDI-MSI circumvents these caveats by generating large sets of imaging spectra, here, we compiled a library of candidates and then utilized LC-MS/MS analysis of serial or adjacent thymic tissue sections, to create a list of candidate peptides detectable in the samples. We subsequently engineered a peak-matching pipeline with a customizable scoring system, to match LC-MS/MS with MALDI-MSI data, and prioritize candidates based on identification confidence and quantification. In summary, this proposed methodology applies the techniques of MALDI-MSI and LC-MS/MS in parallel thymic slide sections, to identify potential protein markers of thymic compartmentalization and endogenous thymic regeneration, using a mouse model of chemotherapy-induced involution. Compared to more routine proteomics experiments, our pipeline combines the identification of potential candidate biomarkers with feasibility assays in a single shot, to assess the capability of MALDI-MSI in confidently quantifying these signals.

METHODS

Mouse Model of Cyclophosphamide-Induced Thymic Involution. FVB/NCrl female mice (n=5), 7-8 weeks old were used for this study. Cyclophosphamide monohydrate (CTX, Thermo Scientific) was reconstituted at a concentration of 25 mg/mL in sterile Phosphate-Buffered-Saline (PBS). Each mouse in the experimental group received an *i.p.* dose of 200 mg/Kg of Cyclophosphamide monohydrate in sterile PBS (200 µL total volume), every 3 days, for a total of 3 doses. The control (vehicle-treated) mouse group received an *i.p.* injection of 200 µL sterile PBS. The last day of chemotherapy treatment was designated as "Day 0". The mice were then blindly categorized into five subgroups. Mice from either control or experimental subgroups were sacrificed on a weekly basis for up to 5 weeks post-chemotherapy i.e., Day 35. Mouse thymi were dissected using standardized autopsy procedures, and were cleaned from peri-thymic adipose tissue, carefully without damaging the thymus. Experiments were replicated in at least three independent mouse cohorts (N=5 mice per group).

MALDI-MSI Analysis of Mouse Thymus Tissue Sections (Fig. 1A). Thymi from vehicle- and cyclophosphamide (Ctx)-treated mice were fixed in 10% Neutral Buffered Formalin for 48h, processed, and paraffin embedded. FFPE thymic tissue sections, cut at 5-µm thickness, were mounted on indium-tin oxide (ITO) conductive glass slides. The FFPE tissue sections were deparaffinized for 1.5 h at 60-65 ^{o}C and washed through a series of xylene, 100%, 95%, 70% ethanol and water. Tissue slides in 10 mM Tris buffer were heated to 95-98 ^{o}C using a steamer for 30 min. Slides were cooled down, buffer exchanged with water, and dried in a desiccator overnight. The tissue slides were then spray-coated with trypsin solution using the TM Sprayer (HTX Technologies). The slides were air dried for 5 min and then incubated in a hydrated chamber for overnight trypsin digestion at 37 ^{o}C. After digestion, slides were dried for 15 min in the vacuum desiccator and then spray coated with CHCA matrix (α-cyano-hydroxycinnamic acid; 5 mg/ml in 50% AcN/0.2% TFA) using the TM Sprayer (HTX technologies).

Peptide spatial mapping was performed by scanning and acquiring spectra m/z range 700-3,500) at 100 µm raster width and 800 laser shots/pixel using the UltrafleXtreme MALDI TOF/TOF mass spectrometer (Bruker Daltonics). After the MALDI imaging analysis, the matrix was washed off from the tissue and followed by staining with Hematoxylin and Eosin (H&E). Spectra were processed by pre-defined smoothing and baseline subtraction. To remove variations in pixel-to-pixel intensities, TIC (mean) normalization was performed by dividing all spectra by the means of all data points. Using Fleximaging v 4.0, unsupervised hierarchical clustering based on Euclidean distance metric and Ward linkage was performed to generate segmentation maps from the images acquired from the tissue samples. The dendrogram was generated with only the top nodes displayed. To delve into additional layers into the dendrogram, the "+" sign was selected to expand the tree. The numbers in brackets corresponded to the number of mass spectra belonging to the same node, while the number before it corresponded to the node ID or the cluster distance. The selected branch generated a display filter assigned to a specific color for clustering pixels with similar spectra. This generated a spatial heatmap that uses a color intensity scale to show the varying intensity ratios of mass signals observed from different areas on the tissue. The initial results obtained from the Ultraflextreme were further assessed by analyzing additional tissue sections from different time points from post-cyclophosphamide treatment using the timsTOF flex mass spectrometer.

Spatial Proteomics. Peptide spatial mapping was performed by scanning and acquiring spectra m/z range of 700-3,500 at 50 µm raster width timsTOF flex mass spectrometer (Bruker Daltonics) equipped with a MALDI-2 laser and Trapped Ion Mobility (TIM). The timsTOF flex use

the SciLs Lab software for data processing to generate peptide ion maps. For timsTOF fleX MALDI-2 data, several built in functions were used to visualize data, including segmentation. To perform segmentation analysis, a feature list was generated by taking the 10,000 most frequent features across all pixels in the entire m/z range, with the most frequent features being present in most pixels, regardless of relative intensity. Features were determined upon importation of the data into SCiLS Lab, where the raw data are binned into features based on the default SCiLS binning parameters, and can be thought of as m/z picked peaks. Segmentation was performed by clustering pixels, using the mass spectra of each pixel across the entire m/z range, using only the features found in the feature list mentioned. The clustering was performed using a bisecting k-means algorithm that utilizes correlation distance as a metric, with each pixel spectrum, both denoised using the weak denoising setting and normalized against the total ion count of the respective pixel. Further statistical analysis was performed using SCiLS Lab's built in 10 principal component analysis using the same 10,000 feature list, normalizing each pixel to the total ion count and scaling the relative intensities of the features to unit variance.

LC-MS/MS and Protein Identification (Fig. 1B). Serial or adjacent FFPE tissue sections at 5 µm thickness were mounted on positively charged regular microscope glass slides. The FFPE tissue sections were deparaffinized for 1.5 h at 60-65 ^{o}C and washed through a series of xylene, 100%, 95%, 70% ethanol and water. Tissue slides in 10 mM Tris buffer were heated to 95-98 ^{o}C using a steamer for 30 min. Slides were cooled down, buffer exchanged with water and dried in a desiccator overnight. The tissue slides were then spray coated with trypsin solution using the TM Sprayer (HTX Technologies). The slides were air dried for 5 min and then incubated in a hydrated chamber for overnight trypsin digestion at 37 ^{o}C. After digestion, slides were dried for 15 min in the vacuum desiccator. The peptides were sequentially extracted twice each by pipetting 30 ul of 0.1% triflouroacetic acid and 60% acetonitrile/ 0.1 triflouroacetic acid, collected and pooled into Eppendorf microcentrifuge tube.

The peptide digests were desalted using C-18 ziptip or Oasis HLB resin by vacuum filtration and eluted with 60% acetonitrile/0.1% TFA, concentrated in a speed vacuum and re-suspended in 0.1% acetonitrile and analyzed by LC-MS/MS using a nanoRSLC U3000 (Dionex, Thermo Scientific) or a nanoAcquity UPLC (Waters) connected to Orbitrap Exploris 480 (Thermo Scientific). The LC gradient is composed of 120 minutes for 4% - 34% solvent B (Solvent A: 0.1% Formic acid and Solvent B: 80% Acetonitrile/0.1% Formic acid).

For peptide identification and label free quantification, the MS/MS data obtained from DDA were searched by the SEQUEST search engine using Proteome Discoverer v2.5 (Thermo Scientific). Protein abundances were transformed into log2 and normalized, and statistical differences between relative protein abundances were assessed using a t-test as previously discussed (Aguilan JT et al, 2020). Automated database search was performed by Proteome Discoverer v2.5 using Sequest search engine. MS/MS data obtained from DDA searched against SwissProt mouse database with the following parameters: missed cleavage = 2; oxidation on M; deamidation on N and Q; peptide tolerance = 10 ppm; MS/MS tolerance = 0.02 Da for MS/MS spectra acquired in the orbitrap analyzer.

PepBridge: The MALDI-MSI and LC-MS/MS Peak Matching Pipeline. For the data obtained from the Ultraflextreme, data obtained from the average spectrum was first processed by reducing the bin size to 4,000 and then converted to a .csv file containing m/z vs. MALDI average intensities. On the other hand, the .csv file from the timsTOF flex was converted to an Excel file and the exported peptide table obtained from the LC-MS/MS analysis was pasted into the same file. The peptide table was sorted by the highest intensity of MALDI peaks and further

processed by an in-house developed program (pepBridge.py) described in detail in **Supplementary Materials & Methods** and **Fig. S3**, which can be downloaded from this link: https://github.com/carlos-madrid-aliste/pepBridge. An m/z with a filter of ± 1.0 Da was used for both the Ultraflextreme and timsTOF flex, in order to match the MALDI m/z with the corresponding theoretical $[M+H]^+$ for each peptide identified from the LC-MS/MS analysis. The MALDI average intensities were then sorted from highest to lowest and plotted. MALDI-LC/MS/MS matches with MALDI average intensities falling below the inflection point of the curve (an arbitrarily assigned noise cut-off filter), were filtered out. Both MALDI average intensities and LC-MS/MS intensities were *log2* transformed. Each *log2* transformed peptide was normalized by the average intensities of all the peptides identified per sample. MALDI-TOF suffers from low resolution and peak widths are broader, when compared to the narrower peaks obtained from high resolution mass spectrometers used for LC-MS/MS, such as the orbitrap. A single peptide peak observed from MALDI-TOF with corresponding peptide ion heat map can potentially match to ≥1 peptide candidate observed from LC-MS/MS. Hence, we validated the results we obtained from the Ultraflextreme using the timsTOF flex mass spectrometer. To provide a basis for ranking of top peptide candidates based on probabilities, we developed a MALDI-LC-MS/MS peak matching pipeline, which served as a (prioritization) scoring system, based on four (4) metrics:

Metric 1: Delta of log2 ratios or log2 fold changes between MALDI and LC-MS/MS. The differences between the *log*2 fold changes of Ctx vs Ctrl between MALDI and LC-MS/MS were calculated and sorted from lowest to highest and plotted against the scores. The highest score, y = 10 corresponded to smallest delta or difference between the *log2* fold changes of "Ctx" vs "Ctrl" obtained from MALDI and LC-MS/MS. Hence, a Gaussian curve was generated with the x centered at 0 *log2* fold change vs. the y maximum of 10. The formula is $f(x) = A \cdot e^{-[(x-\mu)^2/2\sigma^2]}$ where x is the input variable, A is the amplitude, which is the maximum value of the distribution, μ is the mean (or the center) of the distribution, and σ is the standard deviation that controls the spread of distribution. Since A was assigned to be the highest score of 10 and the x = 0 to be at the center, the formula becomes $f(x)=10 \cdot e^{-[(x)^2/2\sigma^2]}$. This was converted to an Excel formula, y = 10*EXP(-A1^2/(2*(B1^2))), where A1 represents the cell containing the input value of x (delta log2 fold change), and B1 represents the standard deviation derived from all the delta log2 fold changes. This formula calculates the y values based on a Gaussian distribution using the specified parameters.

Metric 2: Delta mass between MALDI and LC-MS/MS. The differences between the peptide masses observed from MALDI and LC-MS/MS were calculated. The highest score of y = 100 corresponds to the x with the smallest difference as x approaches 0 while the minimum score of y = 0 corresponds to x with the biggest peptide mass difference observed from MALDI and LC-MS/MS as x approaches 1. The function would be $f(x)=1/1+e^{k(x-x0)}$ where x is the computed delta mass, x0 is the central value where x = 0.5 and k is the steepness parameter. In Excel, the formula is y = 100/(1+EXP(10*(A1-0.5))), where A1 is the computed delta mass, the steepness parameter, k = 10 and central value x = 0.5. This formula calculates the y values based on the negative sigmoid function with the central value x = 0.5.

Metric 3: MALDI intensity. The third metric is the MALDI intensities. The higher the intensity means the higher score where y = 5 as the maximum score while y = 0 is the minimum score vs. x which are the MALDI intensities with a central value of x = 2. So, the function is, $f(x)= 5/1+e -k^{(x-2)}$, where y = 5 is the maximum score, k is the steepness parameter, and x is the MALDI intensity. In Excel, the formula is, y = 5/(1+EXP(-A1+2)), where A1 is the input value, which is the MALDI intensity and the steepness parameter, k = 1. This formula calculates the y values based on the sigmoid function using the specified parameters.

Metric 4: Matching with the image or the peptide ion heat map. The scores from Metrics 1 to 3 are summed, with the highest total representing the top candidate peptide, followed by the other candidate peptides corresponding to a specific MALDI peak (m/z). Metric 4 serves as the final criterion, aligning the peptide's spatial mapping or MALDI molecular image with both the log-fold changes and peptide scores.

Bioinformatic characterization of prioritized candidates. The protein accession numbers of the prioritized candidate proteins were submitted to STRING v12.0 (Szklarczyk D et al, 2023), for functional network association analysis. The network was visualized by confidence meaning of network at medium confidence (0.4), and all active interaction resources were included in the analysis. The k-means clustering approach was selected for classifying the protein subnetworks into thematic clusters involving distinct biological/molecular concepts.

Immunofluorescence. 5 um sections, serial to the ones used for MALDI-MSI analysis, were deparaffinized and dehydrated in double changes of xylene and 100, 95, 70 degrees alcohol, respectively, followed by rehydration. Citrate (Novus Biologicals) and EDTA (Epredia) antigen retrieval was performed with a steamer for 21 min. The blocking step was performed with 5% goat serum (R&D systems) in 0.05% PBS-Tween20 for 1 h, after which slides were incubated with the following primary antibodies overnight at 4°C:, TBCA (Rabbit, polyclonal, Invitrogen), TPR (Rabbit, polyclonal, Invitrogen), KRT5 (Chicken IgY, purified polyclonal, Biologend), KRT8 (Guinea Pig, polyclonal, Origene). All antibodies were used at 1:100, except KRT5, which was used at 1:300. The secondary antibody incubation was performed with the following antibodies at 1:200 dilution for 50 minutes: goat anti-Rabbit Alexa Fluor488 (Invitrogen), goat anti-Chicken IgY Alexa Fluor488 (Invitrogen), goat anti-Guinea Pig Alexa Fluor555 (Invitrogen), followed by nuclear staining for 5 minutes with DAPI (4,6-Diamidino-2-phenylindole dihydrochloride, Novus Biologicals) and mounting with ProLong Gold anti-fade mounting reagent (Invitrogen).

Slides were left to dry overnight at dark, and subjected for digital scanning via a 3D HISTECH P250 Flash III automated slide scanner, using a 20x 0.75NA objective lens into a multichannel overlay image, as described in prior work from our group (Borriello L et al, 2020, Coste A et al, 2020, Karagiannis GS et al, 2017, Sharma VP et al, 2021). All used slides were subjected to the same color adjustment for each marker in CaseViewer version2.4 software.

Histopathology. Hematoxylin and eosin (H&E) staining was conducted with the same deparaffinization procedure as described above, which was then followed by Hematoxylin incubation for 5 min, differentiation for 5 sec, Eosin Y stain for 1 min 45 sec, clearing in 95, then 100 degrees alcohol, and then xylene, and finally mounting with Permount (Fisher Scientific).

RESULTS

Pipeline overview. A graphical summary of the pipeline followed in this work is presented in **Figure 1**. Briefly, FFPE tissue sections are prepared for protein digestion using a TM sprayer and analyzed by MALDI-MSI **(Fig. 1A)**. In parallel, digested peptides from the thymic tissues are collected, dried, and analyzed by LC-MS/MS **(Fig. 1B)**. An integration of these parallel datasets, via our newly developed, customizable algorithm PepBridge **(Suppl. Methods)**, leads to candidate markers of thymic compartmentalization and endogenous regeneration after chemotherapy treatment.

Mouse model of cyclophosphamide-induced thymic involution. We used digital pathology to examine whole slides of murine thymi **(Fig. 2A)**. Under normal conditions, the murine thymus is surrounded by a connective tissue capsule **(Figs. 2A-C)**, which is composed of fibroblasts, blood vessels, and collagen fibers (Moll UM, 1997, Pearse G, 2006, Perez YE & Moran CA, 2022, Suster S & Rosai J, 1990). The capsule invaginates to the organ's interior, forming connective tissue trabeculae, also known as "septae" **(Figs. 2A-D)**, which correspond to the routes of inbound and outbound blood vessels and nerves (Moll UM, 1997, Pearse G, 2006, Perez YE & Moran CA, 2022, Suster S & Rosai J, 1990). These septae segregate the thymus into basic structural/functional units, thymic lobules **(Fig. 2B)** (Moll UM, 1997, Pearse G, 2006, Perez YE & Moran CA, 2022, Suster S & Rosai J, 1990). There are two distinct zones identified within the thymic lobules, an "outer" darker zone, which is characterized by densely packed T lymphocytes and is called "cortex", and an "inner" lighter zone, which is mainly comprised by sparser T lymphocytes and is called "medulla" (Moll UM, 1997, Pearse G, 2006, Perez YE & Moran CA, 2022, Suster S & Rosai J, 1990) **(Figs. 2A-D)**. Thymic compartmentalization via the connective tissue septae is not complete, as the septae never physically interact with one other in the medullary regions. As such, the medulla is often visualized as a single and relatively continuous entity **(Fig. 2A)**, depending on the orientation of the tissue section (Moll UM, 1997, Pearse G, 2006, Perez YE & Moran CA, 2022, Suster S & Rosai J, 1990). A microanatomical region of great functional importance is the corticomedullary junction (CMJ), represented as a relatively distinct border between cortex and medulla **(Fig. 2E)**, in which trabecular vessels branch out, creating the CMJ vessels **(Fig. 2E)** (Moll UM, 1997, Pearse G, 2006, Perez YE & Moran CA, 2022, Suster S & Rosai J, 1990). These vessels are opted for the immigration of early thymocyte progenitors (ETPs) in the thymus, as well as for the egress of mature $CD4^+$ or $CD8^+$ T cells in the peripheral blood (Moll UM, 1997, Pearse G, 2006, Perez YE & Moran CA, 2022, Suster S & Rosai J, 1990).

Acute thymic involution in mice occurs after the administration of cytotoxic agents such as chemotherapy, corticosteroids, antibiotics, and other drugs, and physiologically mimics human responses (Ansari AR & Liu H, 2017, Chaudhry MS et al, 2016, Kinsella S & Dudakov JA, 2020, Lagou MK et al, 2022). Cyclophosphamide (Ctx), an alkylating agent that is often administered in the course of chemotherapy treatment, is an established immunosuppressive drug with deliberating consequences on the thymus (Anton E, 1987, Basta-Kaim A et al, 2001, Erokhina V & Avilova O, 2019, Fletcher AL et al, 2009, Kahri AI et al, 1965, Yoon S et al, 1997). To monitor global proteomic changes during endogenous thymic regeneration after chemotherapy, here, we developed a mouse model of cyclophosphamide-induced thymic involution by exposing female FVB/NCrl mice into radical doses of cyclophosphamide (i.e., 200mg/Kg every 3 days), followed by five weeks of post-chemotherapy monitoring. This experimental pipeline allowed us to capture precise kinetics of endogenous thymic regeneration following the chemotherapeutic insult **(Fig. 2F)**, a process often deemed complex due to the plethora of signaling circuitries regulating thymic remodeling (Dudakov JA et al, 2012, Wertheimer T et al, 2018, Zhan Y et al, 2019). We noted marked thymic involution during the first week following chemotherapeutic

insult, characterized by ambiguous corticomedullary junction and hypoplastic cortex **(Fig. 2G)**. Endogenous thymic regeneration was relatively fast, with thymic mass reaching an equilibrium by the second week following the chemotherapeutic insult **(Fig. 2G)**. Interestingly, there was a relative increase of thymic size by the third and fourth weeks of endogenous thymic regeneration **(Fig. 2G)**, which is consistent with prior observations of "rebound hyperplasia" in human patients receiving chemotherapy (Arpaci T & Karagun BS, 2018, Ayyildiz V et al, 2022, Chen CH et al, 2017, Deniz S et al, 2020, Franke FC et al, 2023, Gulati N & Giulino-Roth L, 2023, Lazaro-Garcia A et al, 2021, Qiu L et al, 2021, Sun DP et al, 2016). Rebound hyperplasia, whose peak was at 3rd week following chemotherapeutic insult (**Fig. 2G)**, was characterized by excessive cortical hyperplasia and a disanalogous medullary compartment, resulting in evident increase of the corticomedullary ratio **(Fig. 2H)**. A "recoil" phase between 4th-5th week following the chemotherapeutic insult, during which thymic size reverted back to its homeostatic size, was captured as the final step of endogenous thymic regeneration **(Fig. 2G)**. Overall, the impact of cyclophosphamide on the murine thymus and the associated kinetics **(Fig. 2G)** are consistent with prior reports (Basta-Kaim A et al, 2001, Fletcher AL et al, 2009, Goldberg GL et al, 2010, Hun ML et al, 2020, Sun L et al, 2015).

Hierarchical clustering of MALDI-MSI acquired spectra from the murine thymus. To identify biomarkers predictive of thymic regeneration, we leveraged the detailed kinetics of endogenous thymic regeneration following Ctx-induced injury. We focused on the 21-day post-Ctx timepoint for several reasons. First, although "rebound hyperplasia" is commonly observed in patients after chemotherapy or other anticancer treatments, no established biomarkers currently gauge thymic functionality during this condition. Second, to our knowledge, a spatially resolved proteome map has never been generated for the regenerating thymus, particularly during rebound hyperplasia. With these considerations, we collected thymi from vehicle-treated (Ctrl) and Ctx-treated mice 21 days after ending their respective treatments **(Fig. 2F)**. The tissues were processed as FFPE samples and subjected to MALDI-MSI following our established pipeline **(Fig. 1A)**. From this analysis, we obtained comprehensive mass-to-charge (m/z) maps, which were processed using Fleximaging v4.1, to extract signals uniquely defining specific regions-of-interest. To correlate these molecular patterns with anatomical features, the same thymic sections used for MALDI-MSI were also stained with H&E. This enabled the direct superimposition of molecular images onto histological structures.

We then performed unsupervised hierarchical clustering of the spectra to identify unique features represented by distinct nodes in the resulting dendrogram **(Fig. S1)**. This approach generated segmentation maps from the acquired tissue images, assigning specific colors to groups of pixels that shared similar spectral signatures. We then extracted three highly unique m/z values that defined each cluster, specifically those at 946 Da, 1337 Da and 1454 Da, and generated their corresponding extracted ion images. Interestingly, each of these three signals represented a different cluster and compartment of the thymus **(Fig. S2)**. Assigning a distinct color to each signal generated individual ion heat maps, which, when overlaid, demonstrated that the spatial relationships among the three signals were preserved. Reconstructing molecular images from the 946 Da, 1337 Da, and 1454 Da signals revealed compartment-specific expression patterns within the thymus **(Figs. 3A-D)**. For example, the 1454 Da signal delineated the thymic capsule, various stromal elements, and surrounding connective tissues **(Fig. 3B)**. The 946 Da signal marked elements expressed predominantly in the medulla, though also present in the cortex **(Fig. 3C)**. In contrast, the 1337 Da signal was expressed throughout the thymus, with a stronger presence in the cortex **(Fig. 3D)**.

Interestingly, some molecular images also revealed differences between normal thymus and thymus undergoing rebound hyperplasia following Ctx insult. The 946 Da signal, for instance,

showed a clear corticomedullary distinction in Ctrl but exhibited a less defined pattern in the Ctx-treated thymus **(Fig. 3C)**. This suggested that the corresponding protein may be reduced or functionally altered during the endogenous regenerative process. In summary, our MALDI-MSI approach accurately mapped thymic compartmentalization, specifically demarcating the thymic capsule and distinct corticomedullary zones, while also revealing histological changes in thymic architecture under experimental conditions.

Our next step was to identify the major discriminating signals uncovered by these analyses. Unsupervised hierarchical clustering of the MALDI-MSI data yielded three major spectral classes, characterized by m/z 946, 1337, and 1454 as distinguishing signals for the thymic medulla, cortex, and capsule regions, respectively (**Fig. 3A–D**). To link these cluster-specific ions to actual proteins, we cross-referenced the m/z values with our LC-MS/MS identifications. Notably, each could be assigned to a peptide: m/z 946 matched the $[M+H]^+$ of a Histone H2A peptide (sequence TKQTAR, monoisotopic 945.54 Da), m/z 1337 corresponded to a peptide from Hemoglobin β-chain (sequence VVAGVANALAHKYH, 1336.73 Da), and m/z 1454 aligned with a tryptic peptide from Thymosin β4 (sequence SDAAVDTSSEITK, 1453.76 Da). These tentative identifications are consistent with the anatomical distribution of the signals, for example, Thymosin β4 is a cytoskeletal G-actin sequestering protein, which is known to be expressed by endothelial cells and stromal cell (e.g., fibroblasts) (Philp D et al, 2006, Smart N et al, 2007, Zuo Y et al, 2013), thus aligning with the strong capsular localization of the 1454 Da ion.

LC-MS/MS proteomics analysis of peptides collected from tissue digestion. One challenge in MALDI-MSI is the assignment of precise identities to the obtained signals. To address this challenge, we performed proteomic analysis of extracted peptides from the tissue slides, which consisted of an online LC-MS/MS using data-dependent acquisition **(Fig. 1B)**. The total number of proteins and peptides for the thymus tissue samples are shown in **Fig. 4A-B**. Identified peptides were label-free quantified for each tissue section corresponding to a time point to determine the fold change enrichment between the treated (Ctx) and vehicle-treated conditions (Ctrl). With this analysis, we obtained a list of identifiable targets present in thymic tissues, which could be subsequently matched to the MALDI-MSI discriminant peaks.

MALDI-LC-MS/MS peak-matching pipeline (pepBridge) combined with a 4-metric scoring system. The major challenge in this step is the issue related to the relatively low resolution of MALDI-TOF mass spectrometry (40,000 at m/z 400) compared to the higher resolution provided by orbitrap mass spectrometry (120,000 at m/z 200) utilized in the LC-MS/MS experiment. With a mass tolerance for MALDI-MSI spectra set at ± 1 Da, it frequently happened that more than 1 peptide candidate identified in the LC-MS/MS runs matched with the potential m/z. For this reason, we developed PepBridge, a MALDI-LC-MS/MS peak matching pipeline based on four rationally-designed metrics based on: (1) delta fold change; (2) delta mass; (3) MALDI intensity and (4) matched image or ion heat map. Each peptide mass identified from LC-MS/MS and matched to MALDI received a score from each metric. The sum of the peptide scores from metrics 1 to 3, were used to rank the probabilities of peptide match. The highest score corresponded to a top candidate peptide with the highest matching probability, and whose sequence belonged to a particular protein. As positive control, we utilized trypsin that was sprayed on the MALDI plate and selected regions of interests at specific locations outside the tissue sections that were expected to contain only trypsin (**Fig. S1 A, A', A" and Fig. S2 A, A'**). Indeed, the PepBridge scoring system revealed that the tryptic peptides were the most enriched, obtaining the highest score and validating our pipeline **(Fig. S4 and Table S1)**.

The imaging data from Veh-treated (Ctrl) and Ctx-treated thymic sections were processed using the PepBridge MALDI-LC-MS/MS peak-matching pipeline. To enable comparison between low- and high-resolution MALDI data, a ±1 Da mass filter was applied. Analysis of the UltrafleXtreme dataset (~15,000 resolving power at m/z 1000) yielded ~23,000 initial MALDI-LC-MS/MS matches. This high number reflected both the relatively low mass resolution of the MALDI-TOF/TOF platform producing broader, less precise m/z peaks than newer systems such as multi-reflectron TOF instruments (Verenchikov et al., 2024) or the timsTOF flex (~200,000 resolution) and the combinatorial nature of the matching process: each MALDI peak (~300–500 per average spectrum) could fall within the ±1 Da tolerance of many of the ~6,500 LC-MS/MS-identified peptides. To refine the list, we removed matches involving low-intensity MALDI peaks (signal-to-noise < 2), reducing the dataset to 676 matches (**Fig. 4D**; **Table S2**). These 676 MALDI peaks each had at least one plausible LC-MS/MS match and were subsequently ranked using our four-metric scoring system (**Fig. 4E-G**). The top-ranked candidates were then carried forward for biological interpretation and validation. When the same tissue sample was analyzed on the higher-resolution timsTOF flex, the initial match count was ~2,500. This was approximately tenfold lower than for the UltrafleXtreme, reflecting reduced peak broadness and ambiguity at higher resolution.

To combine disparate metrics on a common scale, each was transformed into a bounded score (**Fig. 4E-G**). **Metric 1** ($\Delta\log_2$ fold-change between MALDI-MSI and LC-MS/MS) uses a Gaussian function centered at zero, rewarding small discrepancies with higher scores (0-10). While designed for control-treatment comparisons, it can be adapted to any two groups (e.g., region-to-region or PCA clusters) by calculating a pseudo-fold-change. **Metric 2** (mass difference) is scored via a sigmoid (0-100), sharply penalizing offsets >0.1 Da. A ±1 Da tolerance maximized sensitivity but occasionally matched isotopic peaks; such cases were flagged rather than removed to avoid false negatives, especially with lower-resolution MALDI data. With higher-resolution platforms (e.g., timsTOF flex), Metric 2 readily separates isotopes, with false positives scoring near zero. **Metric 3** (MALDI intensity rank) applies a sigmoid (0-5), giving modest weight to signal strength to avoid over-penalizing low-abundance peptides while favoring robustly detectable features. Together, these non-linear transformations ensure that minimal fold-change or mass errors yield near-maximal scores, while larger discrepancies or weak signals sharply reduce confidence. Ultimately, the Peptide Score is the sum of scores from Metrics 1 to 3 for each peptide **(Table S2)**. This corresponds to the rank of the peptide or its matching probability. Interestingly, we found that ranking the peptides within its protein group proved to be more effective in selecting the top peptide candidates by manually comparing the peptide scores and the log-fold changes within a protein group.

In the updated timsTOF flex workflow, **Metric 4** is automated: the top 10 most abundant peptide ion images showing the largest differences between vehicle- (Ctrl) and Ctx-treated samples were selected without manual image review (**Fig. S6**). We retained a ±1.0 Da mass tolerance to maximize sensitivity, though this occasionally resulted in duplicate assignments from isotopic peaks (e.g., both the monoisotopic and +1 Da isotope for Histone H4, Table S2). While more stringent processing such as deisotoping or narrower mass windows could reduce duplicates, these approaches risk false negatives given the current MALDI-MSI resolution. After these filters were applied, the list of candidates was narrowed down to fewer candidates (**Table S3 and Fig. S6**). This to our knowledge, represents the largest spatiotemporally characterized proteome during endogenous thymic regeneration after chemotherapy insult. The protein candidate(s) of interest can be validated by another technique such as immunohistochemistry.

Protein-protein interaction (PPI) analysis reveals three major functional clusters supporting thymic regeneration after cyclophosphamide insult. The candidate proteins identified by PepBridge were analyzed using STRING and grouped by k-means clustering (**Fig. 5**). Most proteins were interconnected, forming three major functional clusters, with a small Fga-F3 pair and eight unconnected proteins (Ubxn1, Tbca, Numa1, Kansl3, Cbr1, Vac14, Rab14, Marcksl1) lying outside the main networks. A few proteins, such as vimentin (Vim), ribosomal protein L7a (Rpl7a), and heterogeneous nuclear ribonucleoprotein M (Hnrnpm), displayed clear "hub-like" activity, consistent with a distributed network topology rather than reliance on a single dominant regulator, in line with previous models of endogenous thymic regeneration (Chaudhry MS et al, 2016, Kinsella S & Dudakov JA, 2020, Velardi E et al, 2021).

Cluster 1 (yellow nodes) includes keratins (Krt5, Krt7, Krt8), vimentin (Vim), proliferation marker Mki67, actin-related proteins (Acta1, Was), myosin heavy chain (Myh9), and regulators such as Rhog and Tgfbi. These proteins maintain thymic stromal scaffolding, especially in cTECs and mTECs, and mediate thymocyte migration and trafficking during regeneration (Ahmad Mokhtar AM et al, 2022, Kadouri N et al, 2020, Kuznetsov NV et al, 2017, Serrador JM et al, 1999, Thompson SB et al, 2022). Some unconnected proteins, such as Marcksl1, have known cytoskeletal roles and may be functionally related despite lacking high-confidence STRING edges (El Amri M et al, 2018).

Cluster 2 (green nodes) centers on ribosomal proteins (Rpl23a, Rps18, Rpl7a, Rpl26, Rpl19, Rps9) and factors such as Pkm, Tkt, Sbds, Srp54b, and Impdh2. These support high translational output and efficient targeting of membrane/secretory proteins, which is essential for TEC and thymocyte proliferation post-injury (Marchingo JM & Cantrell DA, 2022, Sun V et al, 2021). Metabolic enzymes like Pkm and Tkt may reflect shifts in energy demand during tissue repair (Im MJ & Hoopes JE, 1978, Kim E et al, 2023).

Cluster 3 (red nodes) contains RNA-binding proteins (Hnrnpm, Hnrnpab, Hnrnpul1, Elavl1, Rbm15, Puf60) and splicing factors (Srsf2, Srsf5, Thrap3), along with regulators such as Ranbp1, Trim28, and SupT16. These coordinate RNA processing, transport, and alternative splicing, functions critical for reprogramming gene expression during thymic regeneration (Geuens T et al, 2016, Le J et al, 2020, Qi Z et al, 2021, Thibault PA et al, 2021, Zhang H et al, 2024). Proteins like Elavl1 and Trim28 additionally link RNA metabolism to stress response and chromatin remodeling (Ghosh M et al, 2009, Papadaki O et al, 2009, Zhou XF et al, 2012). Overall, the PPI map depicts structural, translational, and RNA-regulatory pathways acting in parallel, underscoring the multifaceted nature of thymic repair.

Validation of MALDI-MSI KRT8 mapping by immunofluorescence. To validate the PepBridge-based MALDI-MSI data, we focused on Keratin 8 (KRT8), a key epithelial marker expressed in both cTECs and mTECs and critical for thymic homeostasis and regeneration (Gupta R et al, 2016, Lee EN et al, 2011, Odaka C et al, 2013). Serial FFPE sections, 5 µm apart from those analyzed by MALDI-MSI, were stained for KRT8 and Keratin 5 (KRT5; mTEC-specific) to co-register molecular and histological data (**Fig. 6A-B**). While minor morphological differences are expected between adjacent sections, overall compartment topology remained consistent. MALDI-MSI revealed KRT8 signal in both cortical ($KRT5^-$) and medullary ($KRT5^+$) regions of Veh- and Ctx-treated thymi, with stronger expression in medulla and no detectable signal in the capsule or perithymic stroma (**Figs. 6A-B**). Immunofluorescence confirmed these patterns: capsule regions showed no KRT8 expression (**Fig. 6C**) and adjacent brown adipose tissue was also $KRT8^-$ (**Fig. 6D**), matching the MALDI-MSI data.

At corticomedullary junctions, both methods showed KRT8 expression in the cortex and medulla, with higher medullary abundance (**Figs. 6E-F**), and MALDI-MSI detected a gradual

signal decrease from medulla to cortex. In some junctions (**Figs. 6G-H**), MALDI-MSI showed a more uniform KRT8 signal across the boundary. Immunofluorescence of these regions revealed denser cTEC meshwork adjacent to the medulla, consistent with active epithelial remodeling. These uniform-signal niches occurred in both treatment groups but were more common after Ctx insult, likely reflecting rebound hyperplasia during regeneration (21 days post-treatment; **Figs. 2F-H**).

Importantly, all the IF validation sites were selected based on MALDI-MSI signal patterns, underscoring the method's sensitivity and specificity in detecting spatial variations in protein expression at corticomedullary boundaries and perithymic zones.

Validation of additional PepBridge-identified proteins by MALDI-MSI and immunofluorescence across thymus compartments. To further confirm the accuracy of PepBridge assignments, we validated additional proteins spanning distinct functional categories. These included nucleoprotein TPR (TPR) and tubulin-folding cofactor A (TBCA; identified in a subset of samples). For each, serial FFPE sections 5 µm apart from those used for MALDI-MSI were subjected to multiplex immunofluorescence, enabling direct comparison of molecular images and histology (**Fig. 7**). TPR, a nuclear basket protein of the nuclear pore complex, was consistently detected in high-resolution timsTOF flex datasets. MALDI-MSI mapped TPR predominantly to medullary regions with lower cortical abundance in both vehicle- and cyclophosphamide-treated thymi (**Fig. 7A-B′**). This distribution was confirmed by immunofluorescence, with nuclear-localized signal enriched in the medulla (**Fig. 7C-D′**). TBCA, a tubulin-folding chaperone important for microtubule assembly, was detected by MALDI-MSI in a subset of samples (**Fig. 7E-E'**When present, TBCA showed higher medullary abundance, confirmed by immunofluorescence (**Fig. 7F-H′**). The variability of TBCA detection across animals may reflect differences in regeneration stage or protein abundance relative to MALDI-MSI sensitivity limits. Together, these results extend our validation beyond KRT8 to include nuclear pore components and cytoskeletal regulators, thus demonstrating the robustness of PepBridge assignments and the ability of MALDI-MSI to capture diverse subcellular localizations and expression patterns across thymic compartments.

DISCUSSION

This study introduces a pipeline for identifying spatially resolved protein biomarkers in the thymus by integrating MALDI-MSI and LC-MS/MS proteomics. By leveraging the complementary strengths of imaging and proteomics, we successfully mapped protein distribution across distinct thymic compartments and identified biomarkers associated with endogenous thymic regeneration following chemotherapy-induced involution. Our findings reveal significant changes in protein expression patterns within the thymic cortex and medulla during rebound hyperplasia. Key markers, including KRT8, TBCA, and TPR, exhibited distinct spatial distributions and dynamic expression profiles, reflecting critical processes involved in thymic remodeling following chemotherapy insult **(Figs. 6-7)**. Of note, KRT8, a prominent intermediate filament protein, which is well-established to be expressed in both cortical and medullary thymic epithelial cells (cTECs and mTECs) (Gupta R et al, 2016, Lee EN et al, 2011), displayed a less defined corticomedullary boundaries in cyclophosphamide-treated mice (Ctx), potentially highlighting defective or ongoing remodeling during the stage of rebound hyperplasia.

Furthermore, our pipeline identified novel markers, such as TBCA, a tubulin-specific chaperone (Cowan NJ & Lewis SA, 2001), which exhibited increased cortical expression during rebound hyperplasia, suggesting a pivotal role for cytoskeletal remodeling in thymocyte proliferation and cortical expansion. Similarly, TPR, a nuclear pore complex protein (Krull S et al, 2010), demonstrated medullary-specific expression under control conditions but was significantly reduced following cyclophosphamide treatment, particularly in medullary thymocytes, emphasizing their vulnerability to chemotherapeutic insults. These findings highlight the potential of TBCA and TPR, as key markers for thymic compartmentalization and regeneration. While several top-scoring assignments were validated via immunofluorescence (e.g., KRT8, TPR, TBCA), we also probed a candidate that did not validate, underscoring the possibility of false positives. In particular, a pepBridge match suggested Keratin 5 (KRT5) for one MALDI-MSI signal (data not shown). However, when we performed IF for KRT5 on serial sections, the observed staining pattern did not correspond to the MSI peptide location. This discrepancy indicated that the original assignment was likely incorrect. Beyond identifying previously underrecognized factors of thymic remodeling, this study is the first to present a spatiotemporally characterized proteome of thymic compartmentalization and recovery. To our knowledge, MALDI-MSI approaches have never before been applied to the thymus, let alone combined with LC-MS/MS proteomics in such a sophisticated and integrative manner. This innovative combination enabled high-confidence protein mapping across thymic compartments, yielding unprecedented spatial resolution of proteomic changes. By leveraging the strengths of both technologies, this approach provides not only a detailed atlas of thymic proteins but also a framework for future studies to explore complex tissue dynamics with enhanced precision and reliability. These advancements position this study as a significant methodological leap forward in understanding thymic regeneration.

Immune and thymic recovery post-chemotherapy is a critical clinical challenge, particularly in pediatric cancer patients, who often experience long-term immune dysfunction due to chemotherapy-induced thymic involution. The thymus plays a central role in T-cell development, and its damage can lead to impaired thymopoiesis, diminished T-cell output, and compromised immune reconstitution. This creates a vulnerability to infections, secondary malignancies, and inadequate immune surveillance, which are significant contributors to morbidity and mortality in pediatric cancer survivors (Lagou MK et al, 2022). Studies like this one address this critical need by providing foundational insights into molecular mechanisms of thymic regeneration, offering potential therapeutic targets and/or functional biomarkers of thymopoiesis. While it is unlikely that MALDI-MSI coupled with LC-MS/MS will be directly implemented in clinical care for pediatric cancer patients (given that thymic biopsy is highly invasive and not part of standard

management) this technology holds great promise in preclinical settings. It could be employed to establish pharmacodynamic biomarkers to monitor immune recovery during cytotoxic treatments in preclinical mouse models (Califf RM, 2018), thereby enhancing the discovery of novel drugs or drug combinations aimed at achieving immunological/thymic recovery post-chemotherapy. For example, proteins such as TBCA and TPR identified in this study and implicated in cytoskeletal remodeling, compartmental stability, and thymic regeneration, could serve as biomarkers for monitoring thymic recovery following cyclophosphamide treatment in animal research. Cyclophosphamide remains a cornerstone chemotherapeutic agent in the management of pediatric malignancies (El Kababri M et al, 2020, Gilheeney SW et al, 2007, Yanagisawa R et al, 2009), and leveraging such biomarkers in preclinical models could provide critical insights to optimize therapeutic strategies and improve long-term immune outcomes for pediatric patients.

Our spatial proteomics platform is broadly applicable beyond thymic mapping. By integrating MALDI-MSI with LC-MS/MS, it enables spatially resolved protein identification in lymphoid organs such as lymph nodes, spleen, thymus, and bone marrow, key sites for immune surveillance, pathogen defense, and hematopoiesis. Mapping proteomes in these tissues can reveal biomarkers and pathways that mediate immune interactions in health and disease. Prior MALDI-MSI studies have indeed mapped immune mediators in infected lymph nodes (Do T et al, 2020), identified metastasis markers in cancer-draining nodes (Mittal P et al, 2016), and profiled lipid changes in injured spleens (Xie P et al, 2024). However, high-resolution protein mapping in complex architectures remains challenging. Our combined approach addresses this by providing confident protein IDs with spatial context, enabling detailed proteomic atlases under conditions such as infection, autoimmunity, and cancer.

pepBridge is designed for widely available MALDI-TOF/TOF instruments, offering high throughput for labs without ultra-high-resolution MSI, while also working with high-resolution data from platforms like the timsTOF flex. It uses a scoring-based strategy that integrates mass accuracy, abundance changes, and intensity ranking to rapidly match MALDI peaks with LC-MS/MS peptides, narrowing candidates for further validation. pepBridge is not a replacement for high-resolution workflows like HIT-MAP, but a bridge to link MALDI-MSI and LC-MS/MS datasets. Protein IDs in our pipeline require at least one confidently matched tryptic peptide, less stringent than conventional proteomics but necessary given the limited peptide coverage of on-tissue digestion. Multiple matched peptides, when present, increase confidence. Current limitations include the lack of formal FDR estimation, as the algorithm always returns a top match. Future versions will integrate decoy-based confidence scoring. Until then, reliability depends on meeting all scoring criteria, which in our tests have been evaluated on a limited but representative dataset.

In conclusion, this study establishes a spatial proteomics pipeline that not only advances our understanding of thymic regeneration but also lays the foundation for broader applications across lymphoid organs. By combining MALDI-MSI and LC-MS/MS with high-confidence protein mapping, this platform offers unparalleled insights into tissue compartmentalization and immune interactions, with the potential to inform therapeutic strategies and improve immune recovery in diverse pathological contexts.

Raw data availability

The mass spectrometry data have been deposited to the ProteomeXchange Consortium via the PRIDE partner repository with the dataset identifier PXD058296. For reviewers to access this dataset please use the token: YhaGeXAUR9tx. Alternatively, reviewers can access the dataset by logging in to the PRIDE website using the following account details:
Username: reviewer_pxd058296@ebi.ac.uk. Password: GZtW9DnfvbEr.

Acknowledgments

The Karagiannis Lab gratefully acknowledges the Montefiore-Einstein Comprehensive Cancer Center for funding through its support grant (P30 CA013330), the Analytical Imaging Facility and its dedicated personnel for the use of the Fast Scanner, acquired via shared instrumentation grants (1S10 OD026852-01A1), and Dr. Maria Lagou for technical support. The Sidoli Lab gratefully acknowledges funding from the Hevolution Foundation (AFAR), the Einstein-Mount Sinai Diabetes Center, and the NIH Office of the Director (S10 OD030286).

Conflict of interest statement

The authors declare no financial conflicts of interest.

References:

Abramson J, Anderson G (2017) Thymic epithelial cells. *Annu Rev Immunol* 35: 85-118. doi:10.1146/annurev-immunol-051116-052320

Aguilan JT, Kulej K, Sidoli S (2020) Guide for protein fold change and p-value calculation for non-experts in proteomics. *Mol Omics* 16: 573-582. doi:10.1039/d0mo00087f

Ahmad Mokhtar AM, Salikin NH, Haron AS, Amin-Nordin S, Hashim IF, Mohd Zaini Makhtar M, Zulfigar SB, Ismail NI (2022) Rhog's role in t cell activation and function. *Front Immunol* 13: 845064. doi:10.3389/fimmu.2022.845064

Alawam AS, Anderson G, Lucas B (2020) Generation and regeneration of thymic epithelial cells. *Front Immunol* 11: 858. doi:10.3389/fimmu.2020.00858

Anderson G, Takahama Y (2012) Thymic epithelial cells: Working class heroes for t cell development and repertoire selection. *Trends Immunol* 33: 256-263. doi:10.1016/j.it.2012.03.005

Ansari AR, Liu H (2017) Acute thymic involution and mechanisms for recovery. *Arch Immunol Ther Exp (Warsz)* 65: 401-420. doi:10.1007/s00005-017-0462-x

Anton E (1987) Delayed toxicity of cyclophosphamide in normal mice. *Br J Exp Pathol* 68: 237-249.

Arpaci T, Karagun BS (2018) Rebound thymic hyperplasia after bone marrow transplantation in children with haemato-oncological diseases. *Contemp Oncol (Pozn)* 22: 95-98. doi:10.5114/wo.2018.75398

Aw D, Silva AB, Palmer DB (2009) Is thymocyte development functional in the aged? *Aging (Albany NY)* 1: 146-153. doi:10.18632/aging.100027

Ayyildiz V, Koksal A, Ogul Y (2022) Rebound thymic hyperplasia secondary to surgical therapy of parotid tumor. *Arch Bronconeumol* 58: 509. doi:10.1016/j.arbres.2021.06.014

Baran-Gale J, Morgan MD, Maio S, Dhalla F, Calvo-Asensio I, Deadman ME, Handel AE, Maynard A, Chen S, Green F, et al (2020) Ageing compromises mouse thymus function and remodels epithelial cell differentiation. *Elife* 9: doi:10.7554/eLife.56221

Basta-Kaim A, Kubera M, Budziszewska B, Roman A, Skowron-Cendrzak A (2001) Effect of physiological and pharmacologically induced thymus involution on the immunoreactivity in c57bl mice. *Pol J Pharmacol* 53: 403-407.

Bhalla P, Su DM, van Oers NSC (2022) Thymus functionality needs more than a few tecs. *Front Immunol* 13: 864777. doi:10.3389/fimmu.2022.864777

Borriello L, Karagiannis GS, Duran CL, Coste A, Oktay MH, Entenberg D, Condeelis JS (2020) The role of the tumor microenvironment in tumor cell intravasation and dissemination. *Eur J Cell Biol* 99: 151098. doi:10.1016/j.ejcb.2020.151098

Buchberger AR, DeLaney K, Johnson J, Li L (2018) Mass spectrometry imaging: A review of emerging advancements and future insights. *Anal Chem* 90: 240-265. doi:10.1021/acs.analchem.7b04733

Cabric V, Brown CC (2023) Thymic mimicry: The art of imitation. *J Exp Med* 220: doi:10.1084/jem.20231010

Cahill RN, Kimpton WG, Cunningham CP, Washington EA (1997) An immune system switch at birth triggers a change in the lifespan of peripheral t cells. *Semin Immunol* 9: 355-363. doi:10.1006/smim.1997.0093

Califf RM (2018) Biomarker definitions and their applications. *Exp Biol Med (Maywood)* 243: 213-221. doi:10.1177/1535370217750088

Chaudhry MS, Velardi E, Dudakov JA, van den Brink MR (2016) Thymus: The next (re)generation. *Immunol Rev* 271: 56-71. doi:10.1111/imr.12418

Chen CH, Hsiao CC, Chen YC, Ko SF, Huang SH, Huang SC, Hsieh KS, Sheen JM (2017) Rebound thymic hyperplasia after chemotherapy in children with lymphoma. *Pediatr Neonatol* 58: 151-157. doi:10.1016/j.pedneo.2016.02.007

Chidgey AP, Boyd RL (2001) Thymic stromal cells and positive selection. *APMIS* 109: 481-492. doi:10.1111/j.1600-0463.2001.apm090701.x

Coste A, Karagiannis GS, Wang Y, Xue EA, Lin Y, Skobe M, Jones JG, Oktay MH, Condeelis JS, Entenberg D (2020) Hematogenous dissemination of breast cancer cells from lymph nodes is mediated by tumor microenvironment of metastasis doorways. *Front Oncol* 10: 571100. doi:10.3389/fonc.2020.571100

Cowan NJ, Lewis SA (2001) Type ii chaperonins, prefoldin, and the tubulin-specific chaperones. *Adv Protein Chem* 59: 73-104. doi:10.1016/s0065-3233(01)59003-8

Deniz S, Susam S, Aksel N, Gayaf M, Guldaval F, Erbaycu AE, Yilmaz U (2020) Effect of rebound thymic hyperplasia on survival in chemotherapy-treated lung cancer. *Turk Thorac J* 21: 303-307. doi:10.5152/TurkThoracJ.2020.18163

Denti V, Mahajneh A, Capitoli G, Clerici F, Piga I, Pagani L, Chinello C, Bolognesi MM, Paglia G, Galimberti S, et al (2021) Lipidomic typing of colorectal cancer tissue containing tumour-infiltrating lymphocytes by maldi mass spectrometry imaging. *Metabolites* 11: doi:10.3390/metabo11090599

Dewez F, Oejten J, Henkel C, Hebeler R, Neuweger H, De Pauw E, Heeren RMA, Balluff B (2020) Ms imaging-guided microproteomics for spatial omics on a single instrument. *Proteomics* 20: e1900369. doi:10.1002/pmic.201900369

Do T, Guran R, Jarosova R, Ondrackova P, Sladek Z, Faldyna M, Adam V, Zitka O (2020) Maldi msi reveals the spatial distribution of protein markers in tracheobronchial lymph nodes and lung of pigs after respiratory infection. *Molecules* 25: doi:10.3390/molecules25235723

Dudakov JA, Hanash AM, Jenq RR, Young LF, Ghosh A, Singer NV, West ML, Smith OM, Holland AM, Tsai JJ, et al (2012) Interleukin-22 drives endogenous thymic regeneration in mice. *Science* 336: 91-95. doi:10.1126/science.1218004

El Amri M, Fitzgerald U, Schlosser G (2018) Marcks and marcks-like proteins in development and regeneration. *J Biomed Sci* 25: 43. doi:10.1186/s12929-018-0445-1

El Kababri M, Benmiloud S, Cherkaoui S, El Houdzi J, Maani K, Ansari N, Khoubila N, Kili A, El Khorassani M, Madani A, et al (2020) Metro-smhop 01: Metronomics combination with cyclophosphamide-etoposide and valproic acid for refractory and relapsing pediatric malignancies. *Pediatr Blood Cancer* 67: e28508. doi:10.1002/pbc.28508

Erokhina V, Avilova O (2019) Ultramicroscopic changes of rats parathyroid glands and thymus after single administration of cyclophosphamide at the different periods of observation. *Wiad Lek* 72: 362-367.

Fata CR, Seeley EH, Desouki MM, Du L, Gwin K, Hanley KZ, Hecht JL, Jarboe EA, Liang SX, Parkash V, et al (2015) Are clear cell carcinomas of the ovary and endometrium phenotypically identical? A proteomic analysis. *Hum Pathol* 46: 1427-1436. doi:10.1016/j.humpath.2015.06.009

Fletcher AL, Lowen TE, Sakkal S, Reiseger JJ, Hammett MV, Seach N, Scott HS, Boyd RL, Chidgey AP (2009) Ablation and regeneration of tolerance-inducing medullary thymic epithelial cells after cyclosporine, cyclophosphamide, and dexamethasone treatment. *J Immunol* 183: 823-831. doi:10.4049/jimmunol.0900225

Franke FC, Damek A, Steglich J, Kurch L, Hasenclever D, Georgi TW, Wohlgemuth WA, Mauz-Korholz C, Korholz D, Kluge R, et al (2023) Differentiation between rebound thymic hyperplasia and thymic relapse after chemotherapy in pediatric hodgkin lymphoma. *Pediatr Blood Cancer* 70: e30421. doi:10.1002/pbc.30421

Geuens T, Bouhy D, Timmerman V (2016) The hnrnp family: Insights into their role in health and disease. *Hum Genet* 135: 851-867. doi:10.1007/s00439-016-1683-5

Ghosh M, Aguila HL, Michaud J, Ai Y, Wu MT, Hemmes A, Ristimaki A, Guo C, Furneaux H, Hla T (2009) Essential role of the rna-binding protein hur in progenitor cell survival in mice. *J Clin Invest* 119: 3530-3543. doi:10.1172/JCI38263

Gilheeney SW, Lyden DC, Sgouros S, Antunes N, Gerald W, Kramer K, Lis E, Meyers P, Rosen N, Thaler HT, et al (2007) A phase ii trial of thalidomide and cyclophosphamide in patients with recurrent or refractory pediatric malignancies. *Pediatr Blood Cancer* 49: 261-265. doi:10.1002/pbc.21045

Goldberg GL, Dudakov JA, Reiseger JJ, Seach N, Ueno T, Vlahos K, Hammett MV, Young LF, Heng TS, Boyd RL, et al (2010) Sex steroid ablation enhances immune reconstitution following cytotoxic antineoplastic therapy in young mice. *J Immunol* 184: 6014-6024. doi:10.4049/jimmunol.0802445

Gonzalez-Fernandez A, Dexter A, Nikula CJ, Bunch J (2023) Nectar: A new algorithm for characterizing and correcting noise in qtof-mass spectrometry imaging data. *J Am Soc Mass Spectrom* 34: 2443-2453. doi:10.1021/jasms.3c00116

Gulati N, Giulino-Roth L (2023) Do no harm: Distinguishing between rebound thymic hyperplasia and hodgkin lymphoma relapse in children. *Pediatr Blood Cancer* 70: e30492. doi:10.1002/pbc.30492

Gupta R, Gupta T, Kaur H, Sehgal S, Aggarwal A, Kapoor K, Sharma A, Sahni D, Singla S (2016) Cytokeratin (ck5, ck8, ck14) expression and presence of progenitor stem cells in human fetal thymuses. *Clin Anat* 29: 711-717. doi:10.1002/ca.22736

Han J, Zuniga-Pflucker JC (2021) A 2020 view of thymus stromal cells in t cell development. *J Immunol* 206: 249-256. doi:10.4049/jimmunol.2000889

Hun ML, Wong K, Gunawan JR, Alsharif A, Quinn K, Chidgey AP (2020) Gender disparity impacts on thymus aging and lhrh receptor antagonist-induced thymic reconstitution following chemotherapeutic damage. *Front Immunol* 11: 302. doi:10.3389/fimmu.2020.00302

Im MJ, Hoopes JE (1978) Transketolase and transaldolase activities in regenerating epithelium during wound healing. *J Surg Res* 25: 50-53. doi:10.1016/0022-4804(78)90157-9

James KD, Jenkinson WE, Anderson G (2021) Non-epithelial stromal cells in thymus development and function. *Front Immunol* 12: 634367. doi:10.3389/fimmu.2021.634367

Kadouri N, Nevo S, Goldfarb Y, Abramson J (2020) Thymic epithelial cell heterogeneity: Tec by tec. *Nat Rev Immunol* 20: 239-253. doi:10.1038/s41577-019-0238-0

Kahri AI, Salmi A, Hannuksela M, Karaharju EO (1965) Histochemistry of rat thymus during involution induced by alkylating agents. *Acta Pathol Microbiol Scand* 64: 441-449. doi:10.1111/apm.1965.64.4.441

Karagiannis GS, Pastoriza JM, Wang Y, Harney AS, Entenberg D, Pignatelli J, Sharma VP, Xue EA, Cheng E, D'Alfonso TM, et al (2017) Neoadjuvant chemotherapy induces breast cancer metastasis through a tmem-mediated mechanism. *Science Translational Medicine* 9: doi:10.1126/scitranslmed.aan0026

Kato S (1997) Thymic microvascular system. *Microsc Res Tech* 38: 287-299. doi:10.1002/(SICI)1097-0029(19970801)38:3<287::AID-JEMT9>3.0.CO;2-J

Kim E, Hwang Y, Kim H, Kim GU, Ryu YC, Yoon M, Choi KY (2023) Pyruvate kinase m2 accelerates cutaneous wound healing via glycolysis and wnt/beta-catenin signaling. *Pharmaceutics* 15: doi:10.3390/pharmaceutics15082028

Kinsella S, Dudakov JA (2020) When the damage is done: Injury and repair in thymus function. *Front Immunol* 11: 1745. doi:10.3389/fimmu.2020.01745

Krull S, Dorries J, Boysen B, Reidenbach S, Magnius L, Norder H, Thyberg J, Cordes VC (2010) Protein tpr is required for establishing nuclear pore-associated zones of heterochromatin exclusion. *EMBO J* 29: 1659-1673. doi:10.1038/emboj.2010.54

Kuznetsov NV, Almuzzaini B, Kritikou JS, Baptista MAP, Oliveira MMS, Keszei M, Snapper SB, Percipalle P, Westerberg LS (2017) Nuclear wiskott-aldrich syndrome protein co-regulates t cell factor 1-mediated transcription in t cells. *Genome Med* 9: 91. doi:10.1186/s13073-017-0481-6

Lagou MK, Anastasiadou DP, Karagiannis GS (2022) A proposed link between acute thymic involution and late adverse effects of chemotherapy. *Front Immunol* 13: 933547. doi:10.3389/fimmu.2022.933547

Lazaro-Garcia A, Lacalle-Gonzalez C, Santonja C, Rodriguez-Pinilla SM, Cornejo JI, Morillo D (2021) Post-chemotherapy rebound thymic hyperplasia mimicking relapse in breast implant-associated anaplastic large cell lymphoma: A case report. *Oncol Res Treat* 44: 196-200. doi:10.1159/000515055

Le J, Park JE, Ha VL, Luong A, Branciamore S, Rodin AS, Gogoshin G, Li F, Loh YE, Camacho V, et al (2020) Single-cell rna-seq mapping of human thymopoiesis reveals lineage specification trajectories and a commitment spectrum in t cell development. *Immunity* 52: 1105-1118 e1109. doi:10.1016/j.immuni.2020.05.010

Lee EN, Park JK, Lee JR, Oh SO, Baek SY, Kim BS, Yoon S (2011) Characterization of the expression of cytokeratins 5, 8, and 14 in mouse thymic epithelial cells during thymus regeneration following acute thymic involution. *Anat Cell Biol* 44: 14-24. doi:10.5115/acb.2011.44.1.14

Lemaire R, Desmons A, Tabet JC, Day R, Salzet M, Fournier I (2007) Direct analysis and maldi imaging of formalin-fixed, paraffin-embedded tissue sections. *J Proteome Res* 6: 1295-1305. doi:10.1021/pr060549i

Manley NR, Richie ER, Blackburn CC, Condie BG, Sage J (2011) Structure and function of the thymic microenvironment. *Front Biosci (Landmark Ed)* 16: 2461-2477. doi:10.2741/3866

Marchingo JM, Cantrell DA (2022) Protein synthesis, degradation, and energy metabolism in t cell immunity. *Cell Mol Immunol* 19: 303-315. doi:10.1038/s41423-021-00792-8

Minato N, Hattori M, Hamazaki Y (2020) Physiology and pathology of t-cell aging. *Int Immunol* 32: 223-231. doi:10.1093/intimm/dxaa006

Mittal P, Klingler-Hoffmann M, Arentz G, Winderbaum L, Lokman NA, Zhang C, Anderson L, Scurry J, Leung Y, Stewart CJ, et al (2016) Lymph node metastasis of primary endometrial cancers: Associated proteins revealed by maldi imaging. *Proteomics* 16: 1793-1801. doi:10.1002/pmic.201500455

Moll UM (1997) Functional histology of the neuroendocrine thymus. *Microsc Res Tech* 38: 300-310. doi:10.1002/(SICI)1097-0029(19970801)38:3<300::AID-JEMT10>3.0.CO;2-R

Mund A, Coscia F, Kriston A, Hollandi R, Kovacs F, Brunner AD, Migh E, Schweizer L, Santos A, Bzorek M, et al (2022) Deep visual proteomics defines single-cell identity and heterogeneity. *Nat Biotechnol* 40: 1231-1240. doi:10.1038/s41587-022-01302-5

Munoz JJ, Garcia-Ceca J, Alfaro D, Stimamiglio MA, Cejalvo T, Jimenez E, Zapata AG (2009) Organizing the thymus gland. *Ann N Y Acad Sci* 1153: 14-19. doi:10.1111/j.1749-6632.2008.03965.x

Nitta T (2022) Mesenchymal stromal cells in the thymus. *Inflamm Regen* 42: 33. doi:10.1186/s41232-022-00219-5

Odaka C, Loranger A, Takizawa K, Ouellet M, Tremblay MJ, Murata S, Inoko A, Inagaki M, Marceau N (2013) Keratin 8 is required for the maintenance of architectural structure in thymus epithelium. *PLoS One* 8: e75101. doi:10.1371/journal.pone.0075101

Ostan R, Bucci L, Capri M, Salvioli S, Scurti M, Pini E, Monti D, Franceschi C (2008) Immunosenescence and immunogenetics of human longevity. *Neuroimmunomodulation* 15: 224-240. doi:10.1159/000156466

Owen JJ, McLoughlin DE, Suniara RK, Jenkinson EJ (2000) The role of mesenchyme in thymus development. *Curr Top Microbiol Immunol* 251: 133-137. doi:10.1007/978-3-642-57276-0_17

Palmer DB (2013) The effect of age on thymic function. *Front Immunol* 4: 316. doi:10.3389/fimmu.2013.00316

Palmer S, Albergante L, Blackburn CC, Newman TJ (2018) Thymic involution and rising disease incidence with age. *Proc Natl Acad Sci U S A* 115: 1883-1888. doi:10.1073/pnas.1714478115

Papadaki O, Milatos S, Grammenoudi S, Mukherjee N, Keene JD, Kontoyiannis DL (2009) Control of thymic t cell maturation, deletion and egress by the rna-binding protein hur. *J Immunol* 182: 6779-6788. doi:10.4049/jimmunol.0900377

Pearse G (2006) Normal structure, function and histology of the thymus. *Toxicol Pathol* 34: 504-514. doi:10.1080/01926230600865549

Perez YE, Moran CA (2022) The thymus: General concepts on embryology, anatomy, histology and immunohistochemistry. *Semin Diagn Pathol* 39: 86-91. doi:10.1053/j.semdp.2021.06.003

Philp D, Scheremeta B, Sibliss K, Zhou M, Fine EL, Nguyen M, Wahl L, Hoffman MP, Kleinman HK (2006) Thymosin beta4 promotes matrix metalloproteinase expression during wound repair. *J Cell Physiol* 208: 195-200. doi:10.1002/jcp.20650

Qi Z, Wang F, Yu G, Wang D, Yao Y, You M, Liu J, Liu J, Sun Z, Ji C, et al (2021) Srsf1 serves as a critical posttranscriptional regulator at the late stage of thymocyte development. *Sci Adv* 7: doi:10.1126/sciadv.abf0753

Qiu L, Zhao Y, Yang Y, Huang H, Cai Z, He J (2021) Thymic rebound hyperplasia post-chemotherapy mistaken as disease progression in a patient with lymphoma involving mediastinum: A case report and reflection. *BMC Surg* 21: 38. doi:10.1186/s12893-021-01048-y

Quanico J, Franck J, Wisztorski M, Salzet M, Fournier I (2017) Combined maldi mass spectrometry imaging and parafilm-assisted microdissection-based lc-ms/ms workflows in the study of the brain. *Methods Mol Biol* 1598: 269-283. doi:10.1007/978-1-4939-6952-4_13

Rane S, Hogan T, Lee E, Seddon B, Yates AJ (2022) Towards a unified model of naive t cell dynamics across the lifespan. *Elife* 11: doi:10.7554/eLife.78168

Serrador JM, Nieto M, Sanchez-Madrid F (1999) Cytoskeletal rearrangement during migration and activation of t lymphocytes. *Trends Cell Biol* 9: 228-233. doi:10.1016/s0962-8924(99)01553-6

Sharma VP, Tang B, Wang Y, Duran CL, Karagiannis GS, Xue EA, Entenberg D, Borriello L, Coste A, Eddy RJ, et al (2021) Live tumor imaging shows macrophage induction and tmem-mediated enrichment of cancer stem cells during metastatic dissemination. *Nat Commun* 12: 7300. doi:10.1038/s41467-021-27308-2

Smart N, Risebro CA, Melville AA, Moses K, Schwartz RJ, Chien KR, Riley PR (2007) Thymosin beta4 induces adult epicardial progenitor mobilization and neovascularization. *Nature* 445: 177-182. doi:10.1038/nature05383

Sun DP, Jin H, Ding CY, Liang JH, Wang L, Fan L, Wu YJ, Xu W, Li JY (2016) Thymic hyperplasia after chemotherapy in adults with mature b cell lymphoma and its influence on thymic output and cd4(+) t cells repopulation. *Oncoimmunology* 5: e1137417. doi:10.1080/2162402X.2015.1137417

Sun L, Sun C, Liang Z, Li H, Chen L, Luo H, Zhang H, Ding P, Sun X, Qin Z, et al (2015) Fsp1(+) fibroblast subpopulation is essential for the maintenance and regeneration of medullary thymic epithelial cells. *Sci Rep* 5: 14871. doi:10.1038/srep14871

Sun Q, Tiziana P, Khan AUM, Heuveline V, Gretz N (2021) A simple optical tissue clearing pipeline for 3d vasculature imaging of the mediastinal organs in mice. *Int J Exp Pathol* 102: 218-227. doi:10.1111/iep.12399

Sun V, Sharpley M, Kaczor-Urbanowicz KE, Chang P, Montel-Hagen A, Lopez S, Zampieri A, Zhu Y, de Barros SC, Parekh C, et al (2021) The metabolic landscape of thymic t cell development in vivo and in vitro. *Front Immunol* 12: 716661. doi:10.3389/fimmu.2021.716661

Suster S, Rosai J (1990) Histology of the normal thymus. *Am J Surg Pathol* 14: 284-303. doi:10.1097/00000478-199003000-00010

Swami S, Tong I, Bilodeau CC, Bourjeily G (2012) Thymic involution in pregnancy: A universal finding? *Obstet Med* 5: 130-132. doi:10.1258/om.2011.110077

Szklarczyk D, Kirsch R, Koutrouli M, Nastou K, Mehryary F, Hachilif R, Gable AL, Fang T, Doncheva NT, Pyysalo S, et al (2023) The string database in 2023: Protein-protein association networks and functional enrichment analyses for any sequenced genome of interest. *Nucleic Acids Res* 51: D638-D646. doi:10.1093/nar/gkac1000

Takahama Y, Ohigashi I, Baik S, Anderson G (2017) Generation of diversity in thymic epithelial cells. *Nat Rev Immunol* 17: 295-305. doi:10.1038/nri.2017.12

Thibault PA, Ganesan A, Kalyaanamoorthy S, Clarke JWE, Salapa HE, Levin MC (2021) Hnrnp a/b proteins: An encyclopedic assessment of their roles in homeostasis and disease. *Biology (Basel)* 10: doi:10.3390/biology10080712

Thompson SB, Waldman MM, Jacobelli J (2022) Polymerization power: Effectors of actin polymerization as regulators of t lymphocyte migration through complex environments. *FEBS J* 289: 6154-6171. doi:10.1111/febs.16130

Tsuji Y, Yamaguchi S, Nakamura T, Ikegawa M (2021) Mass spectrometry imaging (msi) delineates thymus-centric metabolism in vivo as an effect of systemic administration of dexamethasone. *Appl Sci-Basel* 11: doi:ARTN 11038

10.3390/app112211038

Velardi E, Tsai JJ, van den Brink MRM (2021) T cell regeneration after immunological injury. *Nat Rev Immunol* 21: 277-291. doi:10.1038/s41577-020-00457-z

Webb S, Haniffa M (2023) Large-scale single-cell rna sequencing atlases of human immune cells across lifespan: Possibilities and challenges. *Eur J Immunol*: e2250222. doi:10.1002/eji.202250222

Wertheimer T, Velardi E, Tsai J, Cooper K, Xiao S, Kloss CC, Ottmuller KJ, Mokhtari Z, Brede C, deRoos P, et al (2018) Production of bmp4 by endothelial cells is crucial for endogenous thymic regeneration. *Sci Immunol* 3: doi:10.1126/sciimmunol.aal2736

Xie P, Chen J, Dan A, Lin Z, He Y, Cai Z (2024) Long-term exposure to triclocarban induces splenic injuries in mice: Insights from spatial metabolomics and lipidomics. *J Hazard Mater* 480: 136370. doi:10.1016/j.jhazmat.2024.136370

Yanagisawa R, Nakazawa Y, Sakashita K, Tanaka M, Shikama N, Kamijo T, Shiohara M, Koike K (2009) Low toxicity of a conditioning with 8-gy total body irradiation, fludarabine and cyclophosphamide as preparative regimen for allogeneic hematopoietic stem cell transplantation in pediatric hematological malignancies. *Pediatr Transplant* 13: 737-745. doi:10.1111/j.1399-3046.2008.01065.x

Yang H, Youm YH, Vandanmagsar B, Rood J, Kumar KG, Butler AA, Dixit VD (2009) Obesity accelerates thymic aging. *Blood* 114: 3803-3812. doi:10.1182/blood-2009-03-213595

Yoon S, Yoo YH, Kim BS, Kim JJ (1997) Ultrastructural alterations of the cortical epithelial cells of the rat thymus after cyclophosphamide treatment. *Histol Histopathol* 12: 401-413.

Zhan Y, Wang L, Liu G, Zhang X, Yang J, Pan Y, Luo J (2019) The reparative effects of human adipose-derived mesenchymal stem cells in the chemotherapy-damaged thymus. *Stem Cells Dev* 28: 186-195. doi:10.1089/scd.2018.0142

Zhang H, Zhu H, Peng H, Sheng Y (2024) Function of serine/arginine-rich splicing factors in hematopoiesis and hematopoietic malignancies. *Cancer Cell Int* 24: 257. doi:10.1186/s12935-024-03438-7

Zhou XF, Yu J, Chang M, Zhang M, Zhou D, Cammas F, Sun SC (2012) Trim28 mediates chromatin modifications at the tcralpha enhancer and regulates the development of t and natural killer t cells. *Proc Natl Acad Sci U S A* 109: 20083-20088. doi:10.1073/pnas.1214704109

Zuo Y, Chun B, Potthoff SA, Kazi N, Brolin TJ, Orhan D, Yang HC, Ma LJ, Kon V, Myohanen T, et al (2013) Thymosin beta4 and its degradation product, ac-sdkp, are novel reparative factors in renal fibrosis. *Kidney Int* 84: 1166-1175. doi:10.1038/ki.2013.209

FIGURE LEGENDS

Figure 1. Workflow for spatial proteomics analysis of thymic tissues combining MALDI-MSI and LC-MS/MS. (A) Thymic FFPE tissue sections were prepared for MALDI-MSI analysis, including deparaffinization, enzymatic digestion, and matrix coating. MALDI-MSI was performed to acquire spatially resolved molecular signals across tissue sections, generating ion heat maps for distinct protein distributions. **(B)** Parallel FFPE tissue sections were digested, and peptides were extracted for LC-MS/MS analysis using high-resolution Orbitrap mass spectrometry. Identified peptides were label-free quantified to determine fold change enrichments. This workflow enabled the identification and spatial mapping of thymic protein biomarkers, facilitating insights into thymic compartmentalization and regeneration.

Figure 2. Mouse Model of Cyclophosphamide-Induced Thymic Involution. (A-E) The key histological features and compartments of the murine thymus, using Hematoxylin & Eosin (H&E) staining. **(A)** Whole murine thymus, segmented into lobes, lobules through connective tissue capsule and septa, and compartmentalized into outer cortex and inner medulla. **(B)** Magnified insert of the black dotted box in A, revealing a thymic lobule. **(C-D)** Magnified inserts of the black dotted boxes in B, revealing cellular components of the thymic capsule **(C)** or the interlobular septa **(D)**. **(E)** Magnified insert of the white-dotted box in B, revealing cellular components of the corticomedullary junction. **(F)** Pipeline of the mouse model of cyclophosphamide-induced thymic involution. The regenerative process is monitored on a weekly basis following the last dose of chemotherapy (day 0) for up to five weeks (day 35). MALDI-MSI coupled to LC-MS/MS was conducted on day 21, i.e., three weeks following the last dose of chemotherapy. **(G)** Representative H&E sections of whole murine thymi at the distinct timepoints of thymic regeneration after cyclophosphamide insult, as indicated in F. The rebound hyperplasia is notable on days 21 and 28. **(H)** Investigation of thymic lobules during rebound hyperplasia, reveals the maintenance of the overall lobular architecture, albeit with a vast thickening of the lobules, and the disturbed corticomedullary ratio, mostly attributable to increased proliferation of thymocytes in the cortical zone. *CMJ, corticomedullary junction; Veh, vehicle; Ctx, cyclophosphamide.*

Figure 3. Assessing Protein Distribution in Thymic Compartments. (A) Transverse sections of murine thymi from animals receiving either cyclophosphamide (Ctx) or vehicle (Ctrl and then sacrificed three weeks following termination of treatments, and stained with H&E. Dotted black lines indicate various thymic compartments, such as perithymic stroma (s), cortex (c), and medulla (m), identified by their unique histological features. **(B-D)** Molecular images constructed from selected masses show a specific signal at 1454 Da **(B)**, 946 Da **(C)**, and 1337 Da **(D)**. These protein ions signals demonstrate unique and diverse compartmentalization within the thymic structures, with *m/z* 1454 preferentially localized to the thymic capsule and the perithymic stromal tissues **(B)**, while *m/z* 946 **(C)** and *m/z* 1337 **(D)** mostly found in the thymic parenchyma with stronger localization to the medullary or cortical compartments, respectively. However, disturbances in the compartmentalization of the *m/z* 946 and *m/z* 1454 signals is catured in the Ctx-treated thymi, suggesting spatiotemporal changes of the corresponding protein ions. Dotted black boxes in B through D indicate the medullary compartments, as co-registered from the accompanying H&E in A.

Figure 4. Proteomic analysis of thymic peptides from cyclophosphamide-treated and control mice. (A) Total number of proteins and **(B)** peptides identified by LC-MS/MS from thymic tissue sections of cyclophosphamide-treated and vehicle-treated mice. **(C)** Number of MALDI peaks sorted by intensity and matched with LC-MS data (~23,000 matches) before and **(D)** after the filtering with the three scoring criteria of PepBridge (676 peptide matches). **(E-G)** Scoring metrics used in the PepBridge pipeline: **(E)** delta fold change between MALDI and LC-MS/MS, **(F)** delta mass difference, and **(G)** MALDI intensity. Peptides were ranked based on the combined scores from these metrics. The pipeline enabled confident identification of peptide candidates, narrowing the list to 68 high-confidence peptides associated with thymic compartmentalization and regeneration.

Figure 5. Protein-protein interaction (PPI) analysis of 68 candidate proteins, identified through PepBridge in vehicle- and chemotherapy-treated murine thymi. The network was constructed using STRING v12.0(Szklarczyk D et al, 2023). Proteins were organized into distinct color-coded clusters using an in-built feature for k-means clustering. Associations between proteins are visualized using the medium confidence (0.4) modality.

Figure 6. Correlation between MALDI-MSI and KRT5/8 Immunofluorescence. (A-B) KRT8 signal constructed from MALDI-MSI molecular images (left) along with their paired KRT5 and -8 immunofluorescence (right) on the sequential thymic sections of a cyclophosphamide-treated mouse (A), or a vehicle-treated mouse (B). Co-registration reveals mild shifts in the morphology and topography of the tissue, although most compartments can be captured. The yellow-dotted segments shown in the Ctrl animal on the right have been detached during the preparation and the processing of the MALDI-MSI and LC-MS/MS pipelines, and as such do not correspond to any segment on the MALDI-MSI acquisition. Impressively, the remaining component can be co-registered perfectly with the MALDI-MSI acquisition. Small-dotted boxes corresponding to the letters C, D, E, F, G and H, demonstrate the same fields-of-view in the MALDI-MSI acquisitions and the corresponding multiplex-IF sequential slides. **(C-H)** Magnified inserts of the six fields-of-view indicated in the dotted boxes in A and B, assessed by multiplexed immunofluorescence, for DAPI (nuclear stain), Keratin-5 (KRT5) and Keratin-8 (KRT8). C, E, and G correspond to the three fields-of-view in the cyclophosphamide (Ctx)-treated animal. D, F, and H correspond to the three fields-of-view in the vehicle (Ctrl)-treated animal. Hyphenated versions of these images, i.e., C', D', E', F', G', and H' represent magnified inserts of the white-dotted boxes in each corresponding figure, revealing in high-resolution and single-channels (top, KRT5; bottom, KRT8) the cellular details from their parental images. White-dotted lines correspond to the corticomedullary boundaries, as confirmed by KRT5 signal distribution and intensity, with the medulla staining as $KRT5^{high}$ while other compartments as $KRT5^{-}$ or $KRT5^{low}$.

Figure 7. Immunolocalization of Novel Biomarkers of Thymic Compartmentalization in Murine Thymi at Cyclophosphamide-Induced Rebound Hyperplasia. Validation of two novel markers identified through our new MALDI-MSI pipeline, nucleoprotein Tpr (TPR) **(A-D)**, tubulin-specific chaperone-A (TBCA) **(E-H)**. For each immunolabelled protein, a series of sequential representations is reported in a similar manner. The top rows represent cyclophosphamide (Ctx)-treated mice, while the bottom rows (hyphenated versions) represent vehicle (Ctrl)-treated mice. The first column reveals the molecular image of the respective protein, as obtained by MALDI-MSI acquisition, in this case, TPR (A-A') and TBCA (E-E'). The second column reveals the immunolocalization of each respective protein and condition, using multiplex-immunofluorescence in paraffin-embedded tissues, and fields-of-view are representative of at least N=3, in this case, TPR (B-B') and TBCA (F-F'). In all cases, DAPI was used as nuclear stain, to document the presence of tissue, and demarcate the corticomedullary junction (white-dotted lines). C, Cortex; M, Medulla; white-dotted lines indicate corticomedullary junctions. In each image a white line (206 pixels for B, B', and 137 pixels for F, F') crosses through the

corticomedullary junctions and is used for line profiling in the next column. In the third column, the normalized signal intensity of the corresponding protein is plotted along the line profile, in this case, TPR (C-C') and TBCA (G-G'). The black dotted lines indicate the pixel which segments the line into its cortical (left) and medullary (right) side. Intensity values are normalized to the maximum intensity observed from the two line-profiles of the same immunolabelled protein. The line profiles are representations of at least N=20 lines measured in each condition. The fourth and fifth columns represent higher magnifications of the region around the line profiles of the second column. They reveal at cellular detail the precise immunolocalization of each respective protein and condition, using multiplex-immunofluorescence in paraffin-embedded tissues, and fields-of-view are representative of at least N=10, in this case, TPR (D-D'), and TBCA (H-H'). For each example, the fourth column (left) is a merged image including DAPI as a nuclear stain, while the fifth column (right) is a single channel of the corresponding immunolabelled protein. White-dotted lines indicate the corticomedullary junction.

Figure 1

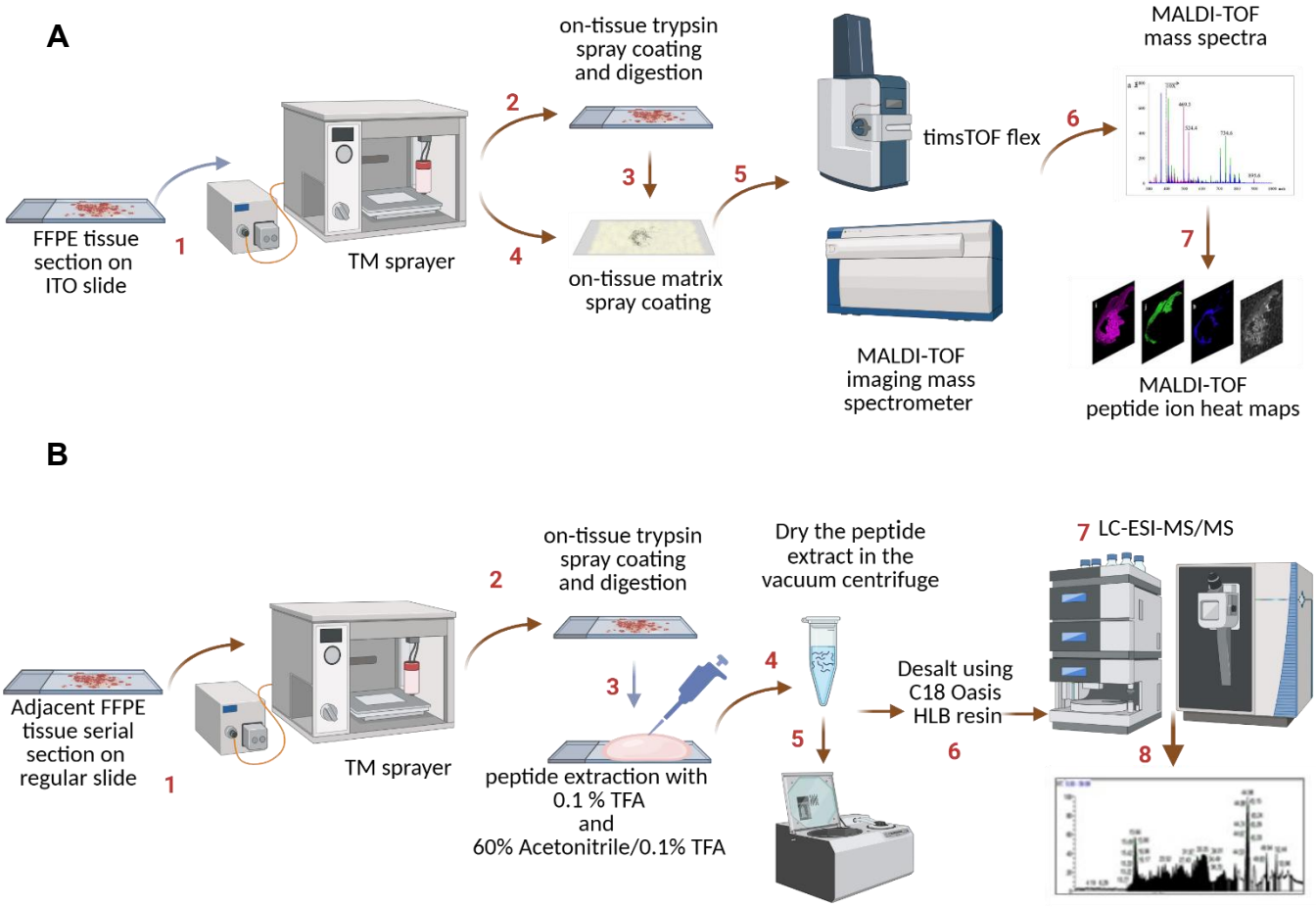
A
FFPE tissue section on ITO slide
1
TM sprayer
2
on-tissue trypsin spray coating and digestion
3
4
on-tissue matrix spray coating
5
timsTOF flex
MALDI-TOF imaging mass spectrometer
6
MALDI-TOF mass spectra
7
MALDI-TOF peptide ion heat maps
B
Adjacent FFPE tissue serial section on regular slide
1
TM sprayer
2
on-tissue trypsin spray coating and digestion
3
peptide extraction with 0.1 % TFA and 60% Acetonitrile/0.1% TFA
4
Dry the peptide extract in the vacuum centrifuge
5
Desalt using C18 Oasis HLB resin
6
7 LC-ESI-MS/MS
8

Figure 2

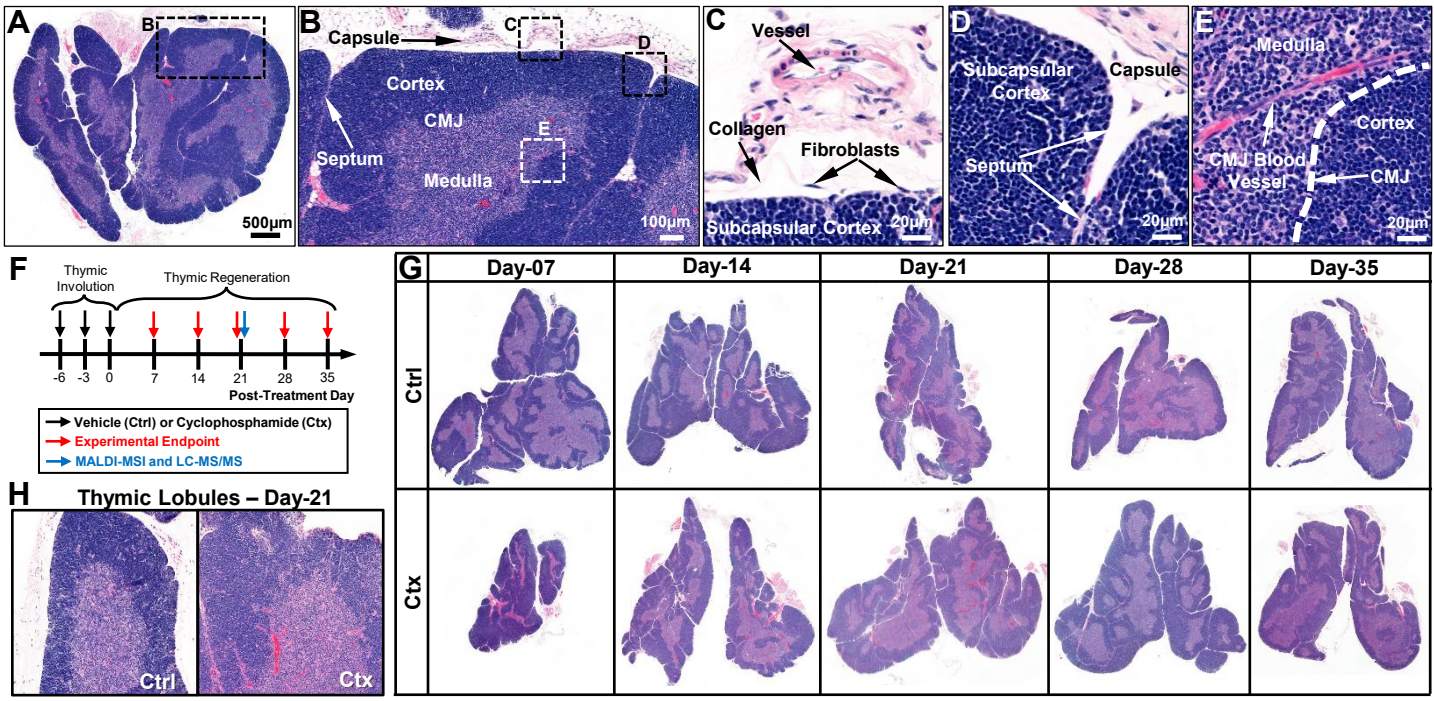
A
B
500µm
B
Capsule
C
D
Cortex
CMJ
E
Septum
Medulla
100µm
C
Vessel
Collagen
Fibroblasts
Subcapsular Cortex
20µm
D
Subcapsular Cortex
Capsule
Septum
20µm
E
Medulla
Cortex
CMJ Blood Vessel
CMJ
20µm
F
Thymic Involution
Thymic Regeneration
-6
-3
0
7
14
21
28
35
Post-Treatment Day
Vehicle (Ctrl) or Cyclophosphamide (Ctx)
Experimental Endpoint
MALDI-MSI and LC-MS/MS
G
Day-07
Day-14
Day-21
Day-28
Day-35
Ctrl
Ctx
H
Thymic Lobules – Day-21
Ctrl
Ctx

Figure 3

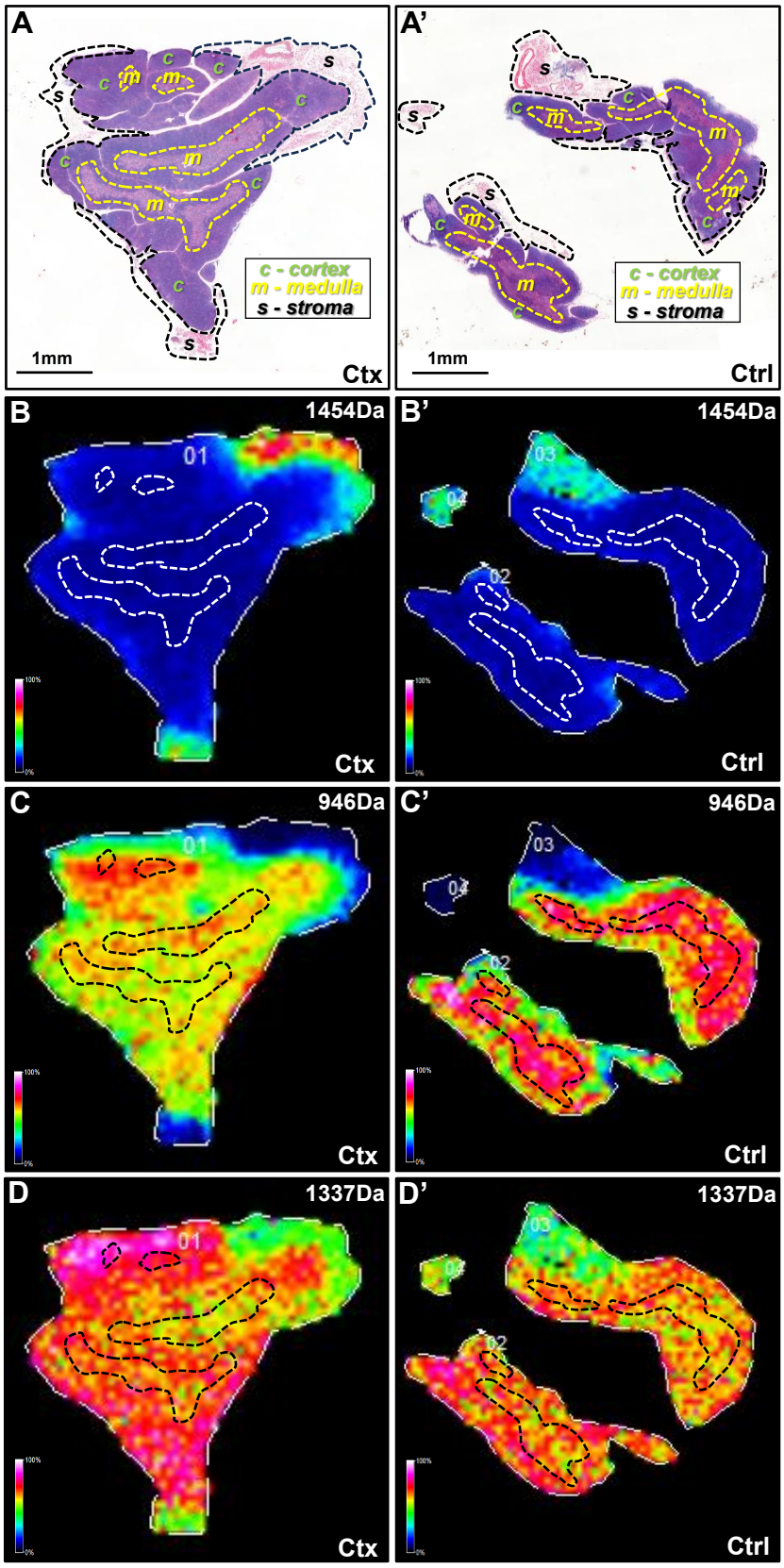
A
A'
c - cortex
m - medulla
s - stroma
1mm
Ctx
Ctrl
B
B'
1454Da
C
C'
946Da
D
D'
1337Da
01
02
03
04

Figure 4

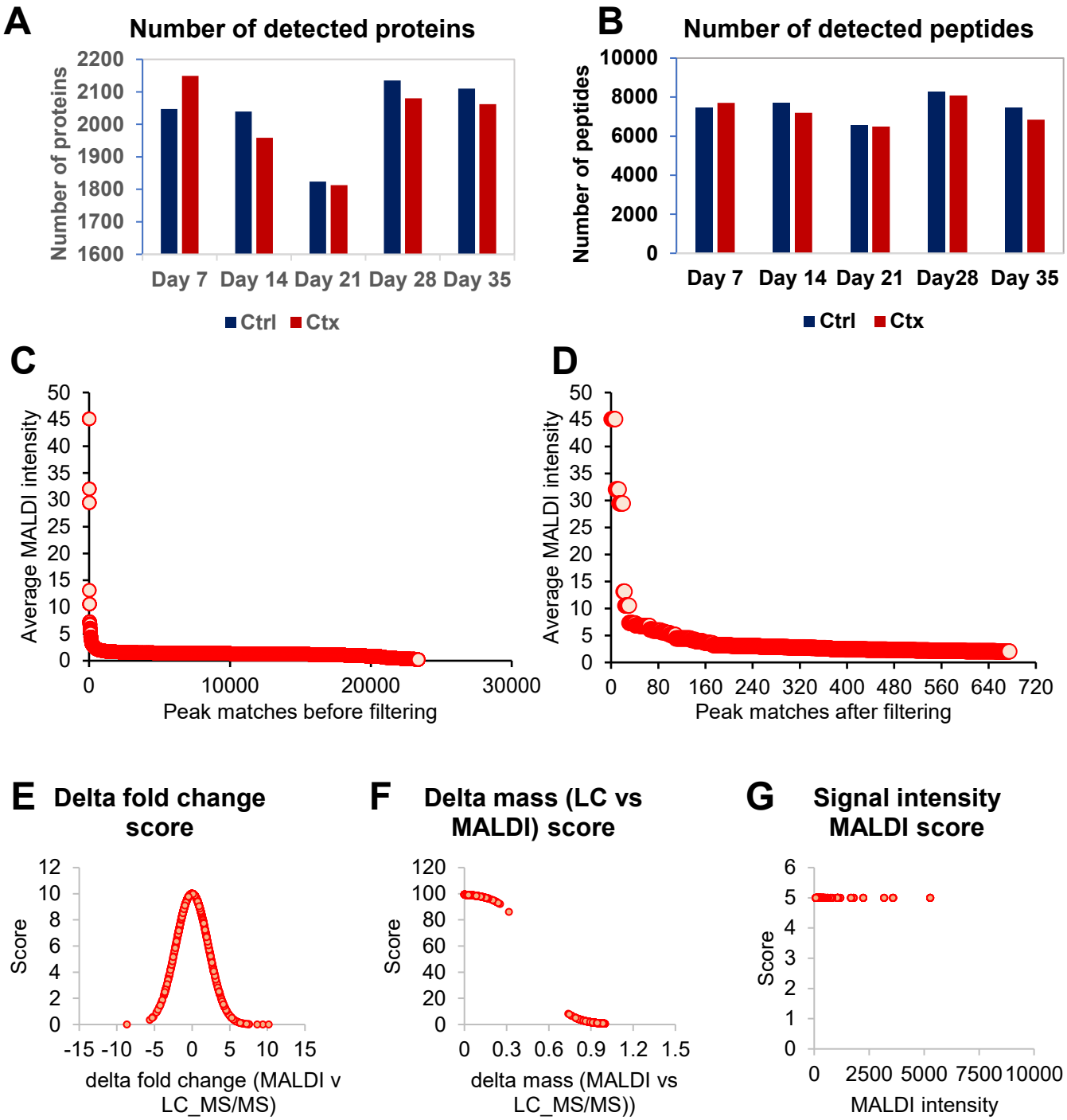
A
Number of detected proteins
Number of proteins
2200
2100
2000
1900
1800
1700
1600
Day 7
Day 14
Day 21
Day 28
Day 35
Ctrl
Ctx
B
Number of detected peptides
Number of peptides
10000
8000
6000
4000
2000
0
Day 7
Day 14
Day 21
Day28
Day 35
Ctrl
Ctx
C
Average MALDI intensity
50
45
40
35
30
25
20
15
10
5
0
0
10000
20000
30000
Peak matches before filtering
D
Average MALDI intensity
50
45
40
35
30
25
20
15
10
5
0
0
80
160
240
320
400
480
560
640
720
Peak matches after filtering
E
Delta fold change score
Score
12
10
8
6
4
2
0
-15
-10
-5
0
5
10
15
delta fold change (MALDI v LC_MS/MS)
F
Delta mass (LC vs MALDI) score
Score
120
100
80
60
40
20
0
0
0.3
0.6
0.9
1.2
1.5
delta mass (MALDI vs LC_MS/MS))
G
Signal intensity MALDI score
Score
6
5
4
3
2
1
0
0
2500
5000
7500
10000
MALDI intensity

Figure 5

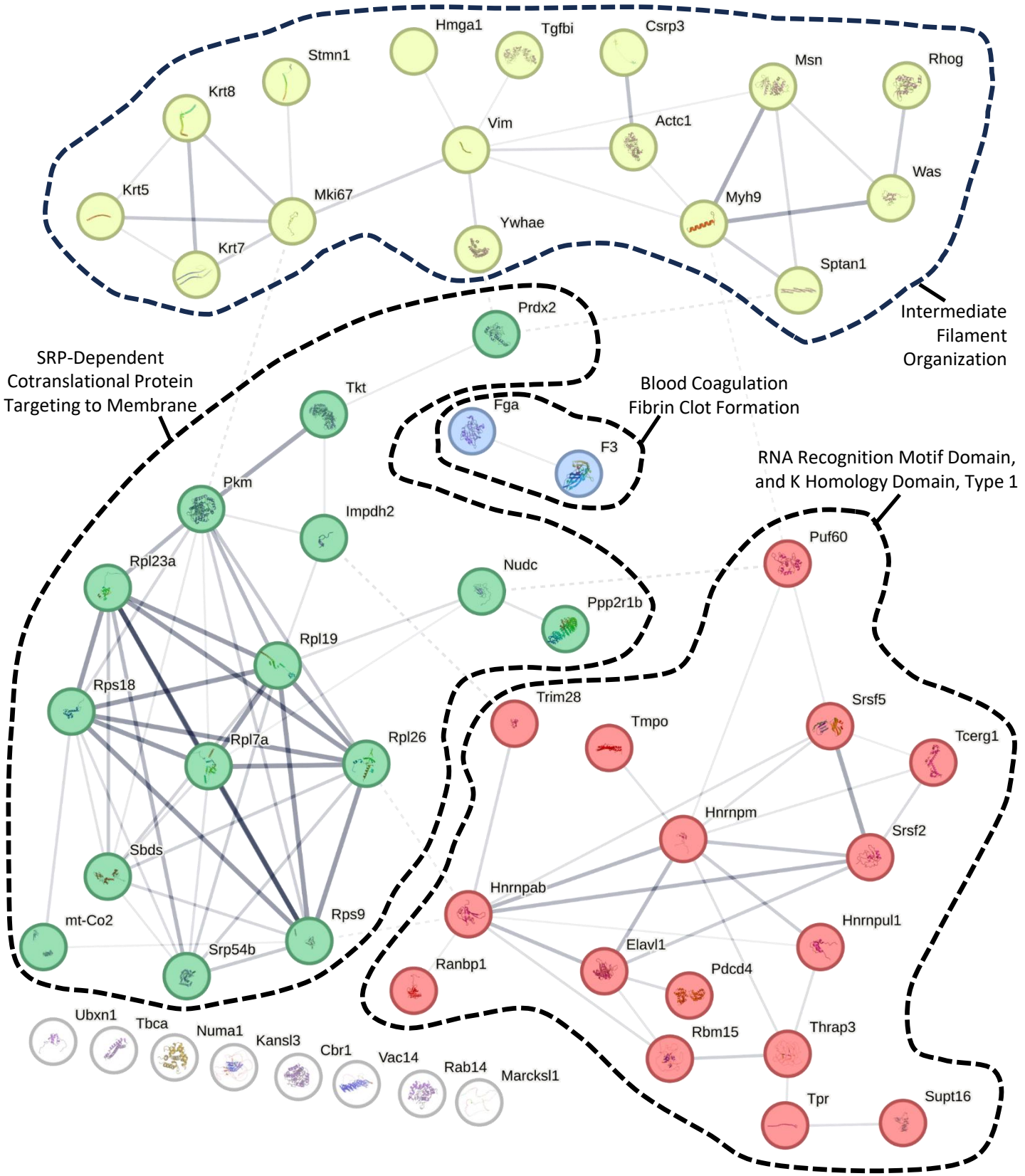
Hmga1
Tgfbi
Csrp3
Stmn1
Msn
Rhog
Krt8
Vim
Actc1
Was
Krt5
Mki67
Myh9
Ywhae
Krt7
Sptan1
Intermediate Filament Organization
Prdx2
SRP-Dependent Cotranslational Protein Targeting to Membrane
Tkt
Fga
Blood Coagulation Fibrin Clot Formation
F3
RNA Recognition Motif Domain, and K Homology Domain, Type 1
Pkm
Impdh2
Puf60
Rpl23a
Nudc
Ppp2r1b
Rpl19
Rps18
Trim28
Srsf5
Tmpo
Rpl7a
Rpl26
Tcerg1
Hnrnpm
Srsf2
Sbds
Hnrnpab
Rps9
Hnrnpul1
mt-Co2
Elavl1
Srp54b
Ranbp1
Pdcd4
Ubxn1
Tbca
Numa1
Kansl3
Cbr1
Vac14
Rab14
Marcksl1
Rbm15
Thrap3
Tpr
Supt16

Figure 6

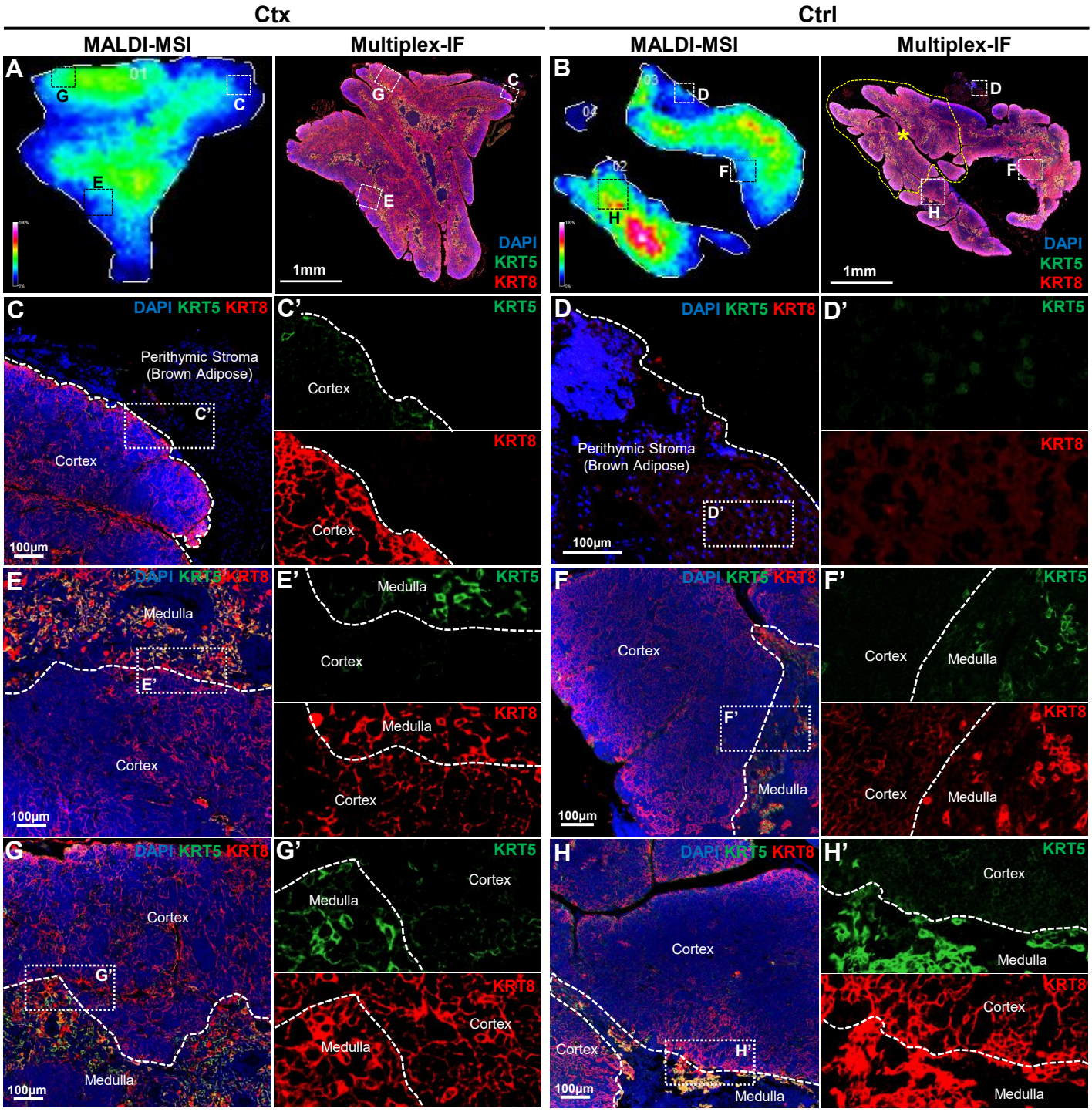
Ctx
Ctrl
MALDI-MSI
Multiplex-IF
MALDI-MSI
Multiplex-IF
A
B
C
C'
D
D'
E
E'
F
F'
G
G'
H
H'
DAPI KRT5 KRT8
KRT5
KRT8
1mm
100µm
Perithymic Stroma
(Brown Adipose)
Cortex
Medulla

Figure 7

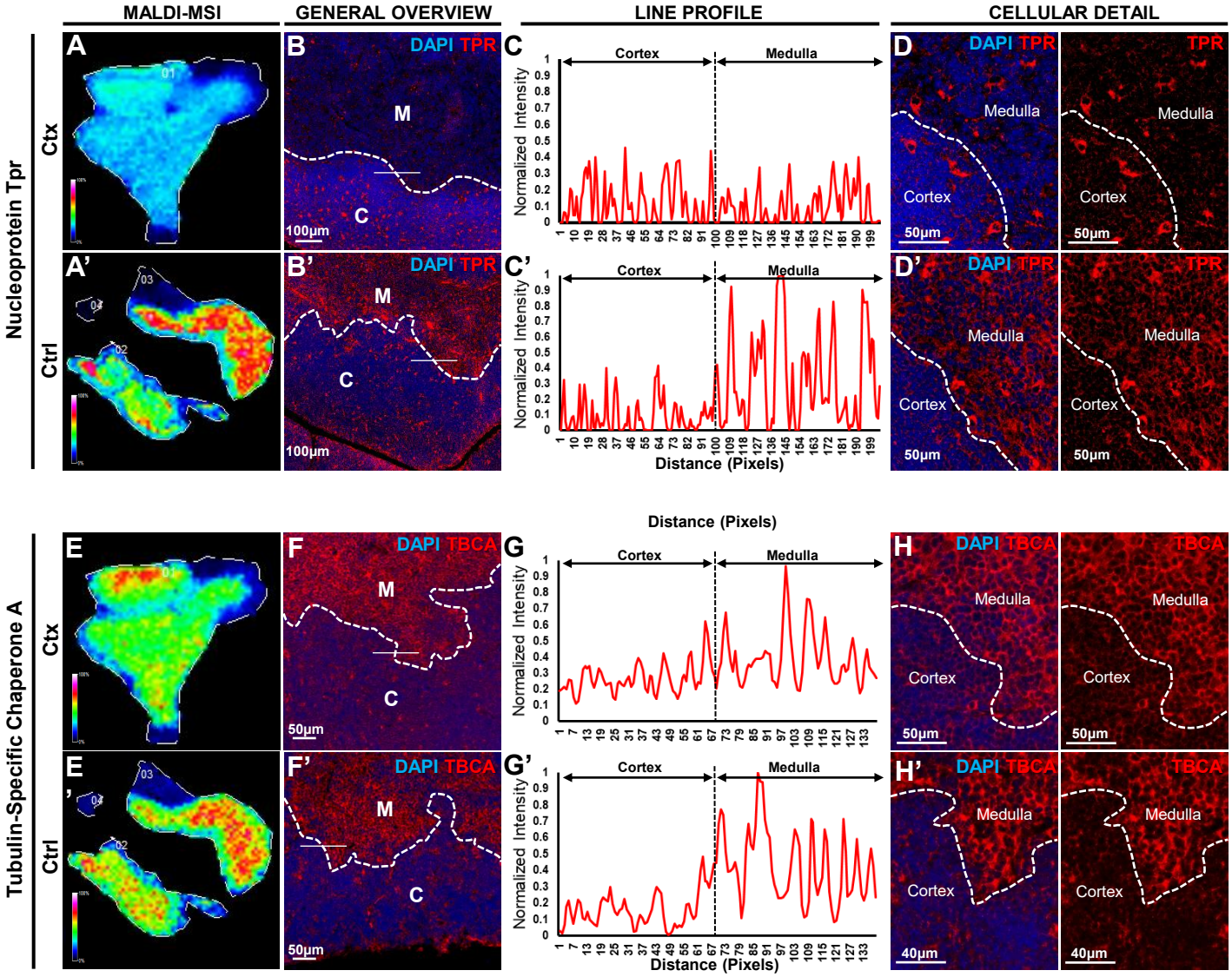
MALDI-MSI
GENERAL OVERVIEW
LINE PROFILE
CELLULAR DETAIL
Nucleoprotein Tpr
Ctx
Ctrl
A
A'
B
B'
C
C'
D
D'
DAPI TPR
TPR
M
C
100µm
Cortex
Medulla
Normalized Intensity
Distance (Pixels)
50µm
Tubulin-Specific Chaperone A
E
E'
F
F'
G
G'
H
H'
DAPI TBCA
TBCA
40µm